Mechanical Systems and Signal Processing 185 (2023) 109827

Contents lists available at ScienceDirect

Mechanical Systems and Signal Processing

journal homepage: www.elsevier.com/locate/ymssp

Morton effect prediction with validation using a CFD based CNN for pad inlet temperatures

Jongin Yang [a,b], Alan Palazzolo [b,*]

[a] Korea Atomic Energy Research Institute, 989-111 Daedeok-daero, Yuseong-gu, Daejeon 305-353, Republic of Korea
[b] Department of Mechanical Engineering, Texas A&M University, College Station TX77840, United States

ARTICLE INFO

Keywords:
Morton effect simulation
Dynamic thermal-fluid-structural interaction analysis
Groove mixing
Deep learning
CFD

ABSTRACT

The Morton Effect (ME) is a thermal-fluid–structure interaction instability occurring in rotating machinery supported by hydrodynamic journal bearings. The mechanism of ME consists of a bowed rotor or mass imbalance induced shaft synchronous whirl vibration in the bearing, which causes local, asymmetric heating of the journal, which causes shaft bending, potentially leading to increasing vibration. This study presents an original ME simulation approach that includes a CFD (Computational Fluid Dynamics) bearing groove model, embedded in a deep learning algorithm for computational efficiency and non-expert usage. The groove model provides a 2D oil temperature distribution at the leading edge of the bearing pads, yielding a more accurate journal axisymmetric temperature distribution which is the source of the ME. The paper provides validation of the approach by test result correlation, and illustrates the effects of parameter variation and configuration variation, by examining various oil injection types. The approach may be used for correcting ME occurring in existing machinery, or for designing machinery to avoid the ME.

1. Introduction

The ME is a thermally induced, shaft synchronous vibration instability. It frequently occurs, where the rotor supported by hydrodynamic bearings has a large overhung mass and spins at high rpm, as shown in Fig. 1(a). As depicted in Fig. 1(b), the primary cause of the ME is the rotor's thermal bending caused by asymmetric heating of the shaft journal, due to the synchronous shaft vibration orbit in the bearing. The mechanical imbalance typically produces the synchronous vibration illustrated with two half-periods as in Fig. 1(c). In the ME phenomena, the heavy spot (mechanical or initial imbalance) leads the high spot. Asymmetric heating of the journal from shearing of the lubricant is characterized by a sinusoidal circumferential temperature distribution. The difference between the min and max temperatures on the journal surface is referred to as the "circumferential ΔT (or just ΔT)" in this study. The hot spot (max temperature) lags behind the high spot (min film thickness) due to the convective effect in the fluid-film. The thermal bow is located approximately 180 deg from the hot spot. Fig. 1(c) shows the ME ΔT caused by the synchronous vibration, resulting from excitation by the resultant of the original mechanical imbalance and the induced thermal bow. This mechanism may form a positive feedback loop resulting in unacceptable levels of vibration.

Simulating the nonlinear and complex multiphysics nature of ME is ideally performed with a high fidelity computational model capturing all of its conjugate heat transfer, flow, thermal deflection and vibrational aspects. However, practical computational limits have made this an elusive goal. Thus, from its original discovery by Morton [1] and Hesseborn [2], approximate models have been

* Corresponding author.
E-mail address: a-palazzolo@tamu.edu (A. Palazzolo).

https://doi.org/10.1016/j.ymssp.2022.109827
Received 16 March 2022; Received in revised form 15 August 2022; Accepted 20 September 2022
Available online 27 September 2022

Nomenclature

T	Temperature, deg C
Q	Flowrate, m^3/s
η	Non-dimensional temperature
η_k	Constant-MC
η_{2D}	2D-MC
p	Static pressure, Pa
ρ	Density, kg/m^3
μ	Dynamic viscosity, Pa•s
λ	Thermal conductivity, W/(m•K)
h_l	Film thickness, m
U_s	Shaft surface velocity, m/s
R_s	Shaft radius, m
$h_{p,TE}$	Film thickness change by pad thermal deformation, m
$h_{j,TE}$	Film thickness change by journal thermal deformation, m
c_p	Specific heat, J/(kg•K)
$\overrightarrow{U}$	Fluid velocity vector with u, v, and w, m/s
x_R	Journal center position × coordinate, m
y_R	Journal center position y coordinate, m
$C_{l,p}$	Radial pad clearance, m
$C_{l,b}$	Radial bearing clearance, m
θ_x	Journal pitch motion coordinate, deg
θ_y	Journal yaw motion coordinate, deg
x_{pvt}	Pad pivot deformation, m
δ_{tlt}	Pad tilting motion coordinate, deg
α_{pit}	Pad pitch motion coordinate, deg
θ_p	Pad angular position, deg
α	Viscosity coefficient, 1/deg C
$e_{bw,i}$	Thermal imbalance magnitude for rotor's node i, m
$\theta_{bw,i}$	Thermal bow magnitude for rotor's node i, deg
$\varphi_{bw,i}$	Thermal imbalance phase angle for rotor's node i, deg
$\psi_{bw,i}$	Thermal bow phase angle for rotor's node i, deg
$\{x_t\}$	Rotor's total displacement vector, m
$x_{R,i}$	Rotor's × displacement for node i, m
$y_{R,i}$	Rotor's y displacement for node i, m
$\theta_{Rx,i}$	Rotor's × angular displacement for node i, deg
$\theta_{Ry,i}$	Rotor's y angular displacement for node i, deg
$[M_R]$	Rotor's mass matrix, kg
$[K_R]$	Rotor's stiffness matrix, N/m
$\{x_r\}$	Rotor's relative displacement, m
$\{F_{gs}\}$	Rotor's gyroscopic force vector, N
$\{F_{lb}\}$	Rotor's linear bearing force vector, N
$\{F_{im}\}$	Rotor's imbalance force vector, N
$\{F_{nb}\}$	Rotor's non-linear bearing force vector, N
$\{F_{bw}\}$	Rotor's thermal bow force vector, N
$[C_{gs}]$	Rotor's gyroscopic damping matrix, Ns/m
$[C_{lb}]$	Rotor's linear bearing damping matrix, Ns/m
$[K_{lb}]$	Rotor's linear bearing stiffness matrix, N/m
$m_{im,i}$	Rotor's mechanical imbalance weight mass for node i, kg
$e_{im,i}$	Rotor's mechanical imbalance magnitude for node i, m
$\varphi_{im,i}$	Rotor's mechanical imbalance phase angle for node i, deg
$F_{fx,i}$	Non-linear bearing fluidic × force for node i, N
$F_{fy,i}$	Non-linear bearing fluidic y force for node i, N
$m_{R,i}$	Rotor mass for node i, kg
$I_{T,i}$	Rotor transverse mass moment of inertia for node i, kgm^2
ω_R	Rotor spin frequency, rad/s
M_{PG}	Pad mass, kg

I_G	Pad moment of inertia, kgm^2
$F_{nx,i}$	Pivot direction force from nodal normal force on pad surface, N
$F_{tx,i}$	Pivot direction force from nodal tangential force on pad surface, N
$M_{n,i}$	Pad moment from nodal normal force on pad surface, Nm
$M_{t,i}$	Pad moment from nodal tangential force on pad surface, Nm
D_g	Nozzle or orifice diameter, m
P_t	Total pressure at supply oil inlet, Pa
L_b	Bearing length, m
U_s	Shaft surface velocity, m/s
P_{in}	Groove circumferential inlet pressure, Pa
T_{in}	Groove circumferential inlet temperature, degC
h_{in}	Groove circumferential inlet height, m
P_{out}	Groove circumferential outlet pressure, Pa
h_{out}	Groove circumferential outlet height, m
h_s	Seal height, m
W_g	Groove width (circumferential length), m

Subscripts

in	Groove circumferential inlet
out	Groove circumferential outlet
sup	Supply oil inlet
l	Liquid (or fluid)
s	Shaft (or solid)
o	Reference value

Acronyms

CFD	Computational Fluid Dynamics
DOE	Design of Experiment
RANS	Reynolds Averaged Navier Stokes
RMSE	Root Mean Squared Error
SST	Shear Stress Transport
LHS	Latin Hypercube Sampling
ME	Morton Effect
MC	Mixing Coefficient
TPJB	Tilting Pad Journal Bearing
TEHD	Thermo-Elasto-Hydro-Dynamic
dofs	Degrees of freedom
FVM	Finite Volume Method
FEM	Finite Element Method

devised to aid in understanding ME and to provide tools to remedy it in existing machines, or avoid at in the machinery design stage. Morton and Keogh [3] proposed a ME prediction model employing classical feedback theory, indicating ME occurrence by the sign of a gain parameter. Their work employed short bearing theory with a 2D energy equation and a constant viscosity assumption for the fluid film. The journal and bearing are modeled with a 2D energy equation. The ΔT is evaluated by an orbit perturbation method. Coupling of the time-varying orbit effect with the thermal bending was considered in their later work [4]. Gomiciaga and Keogh [5] utilized CFD, and thermal analysis for the journal, fluid, and bearing for several predefined orbit points. The heat flux obtained at all points was averaged to get the journal temperature distribution for the orbit. A steady state analysis was employed for a given orbit in a fixed, circular bearing.

Balbahadur and Kirk [6,7] presented an equivalent imbalance level threshold criterion to indicate occurrence of the ME rotor instability. This was regarded as occurring when the resultant imbalance (original mechanical imbalance + thermal bow induced imbalance) exceeds an imbalance level (threshold criterion), that causes the resulting centrifugal force to exceed 15 % of the total rotor weight at the max operating speed. A linear velocity profile is assumed, and a 1D energy equation is solved for the fluid-film model. The thermal defection, which is calculated by a simple formula with ΔT, was used to determine the thermal unbalance. It was assumed that high and hot spots correspond. Childs and Saha [8] decomposed the elliptical vibration orbit into forward and backward whirling circular orbits. The ΔT for the circular orbits were calculated offline and stored in lookup tables. The $\Delta\Delta T$ in the system simulation was then conducted by interpolating the ΔT's fetched from the lookup table during the iterative system response solution. Journal thermal bending was obtained by handbook deflection formulas and the instantaneous ΔT. The bending changed the equivalent imbalance of an overhung disc, which in turn was used to update the steady state imbalance response prediction.

Several researchers [9–11] have furthered ME simulation sophistication with higher dimension models. Suh and Palazzolo [9–10] developed ME simulation models with 3D fluid-film, rotor, and bearing sub-models, for pressure and temperature prediction. The rotor

and bearing structural models provide thermal deformations, and thermal bending induced imbalance is distributed between the overhung mass and bearing nodes in the rotordynamic model. This modeling approach was extended by Tong and Palazzolo [11], by replacing the thermal bending induced equivalent imbalance, with a more exact thermally induced rotor bow model. In addition, Plantegenet et al. [12–13] presented an excellent experimental study for the ME with plain journal and flexure pivot journal bearings.

References [9–11] advanced ME effect modeling sophistication, however they employed a bulk flow, approximate mixing model for providing uniform leading edge film temperature boundary conditions. This is of key importance since the journal temperature distribution, which is the origin of the ME, may be heavily influenced by the leading edge, temperature boundary conditions. CFD studies reveal the complex nature of the flow convective effect between the prior pad's trailing-edge and the next pad's leading-edge. The film temperature distribution at the pad leading-edge is significantly affected by the flow convective effect and possesses significant gradients in the radial and axial directions. These gradients influence the journal surface heat flux and its resulting circumferential temperature distribution. Full CFD studies reveal the inadequacy of past ME simulation models, which impose a constant MC (film temperature), i.e. zero radial and axial heat flux, at the pad leading edges, resulting in inaccurate heat fluxes on the journal surface. Here, the ability of the 2D-MC deep learning method to provide calculated 2D film temperature distributions at the pad leading-edges, yields major advantages in model accuracy, and eliminates the guesswork of selecting a MC.

Fig. 2 depicts the computational domains for the rotor-bearing system, showing groove regions between the bearing pads. The pad film temperature at its leading edge is prescribed and is referred to as "fluid-film leading-edge temperature". The fluid-film leading-edge temperature has a strong influence on the journal temperature distribution (ΔT) due to the journal's fast rotation (intense advection heat).

{Fig. 2}.

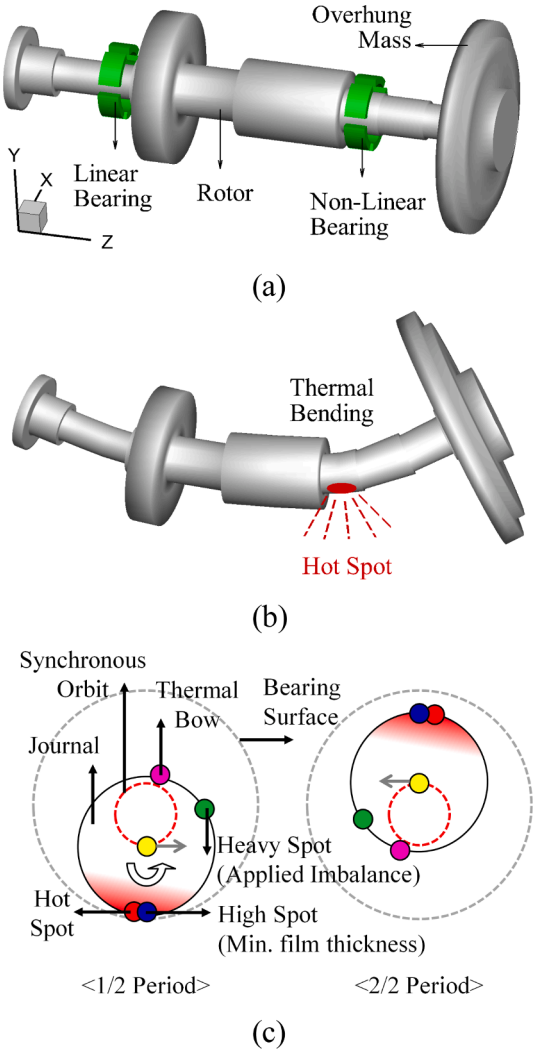

Fig. 1. Illustration for ME in a rotor-bearing system; (a) rotor-bearing system, (b) thermal bending, (c) cyclic asymmetric heating with heavy, high, hot spots, and thermal bow.

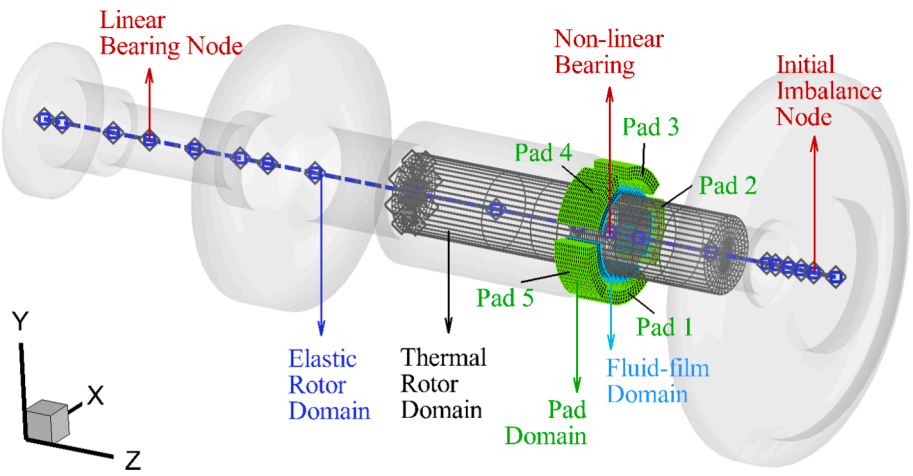

Fig. 2. Computational domains (31,478 nodes, counter-clockwise rotation).

References [9,14–15] utilize the conventional uniform-MC (Mixing Coefficient) approach for prescribing fluid-film leading-edge temperature. This approach can be generalized by.

$$\eta(r,z) \equiv \frac{T_{out}(r,z) - T_{sup}}{T_{in} - T_{sup}} = f(Q_{in}, Q_{out}, \eta_k, \ldots) \tag{1}$$

where (η) is a non-dimensional temperature, the constant-MC (η_k) is assumed from 0.4 to 1.0, T_{sup} is the supply oil flowrate, T_{in} and Q_{in} are the prior pad's fluid-film trailing-edge temperature and flowrate. Q_{out} and T_{out} indicate the next pad's fluid-film leading-edge temperature and flowrate.

Traditional constant MC models neglect the axial and radial temperature variation at the film entrance into the leading edge of a pad. Yang and Palazzolo [16–17] confirmed that the constant MC approach was limited in predicting the journal temperature distribution reliably. A summary of the evolution of tilt pad journal bearing mixing models is included for the interested reader in Ref. [18].Journal temperature is a very important parameter in the ME simulation, due to its effect on rotor bow. The researchers presented the 1D-MC approach that can account for the axial fluid-film leading-edge temperature distribution via the CFD-informed machine learning. The 1D-MC approach was limited to one oil injection type with one orifice or nozzle. A 2D-MC approach employing a deep convolutional autoencoder neural network for the CFD-data training, and developed for various injection types, was presented in their succeeding work [19]. The 2D-MC approach provides the 2D fluid-film leading-edge temperature distribution for various oil injection types. This was applied for static response and dynamic force coefficients predictions of a Tilting Pad Journal Bearing (TPJB), but not for the ME simulation.

The main purpose of this study is to extend the 2D-MC-deep learning approach to accurate simulation of the ME. This is a pioneering application of deep learning, for predicting shaft asymmetric temperature prediction, utilizing the FVM (Finite Volume Method). The ME vibration response, journal ΔT, and shaft thermal bow are determined for various oil injection types and supply oil flowrates. Limitations of the conventional MC model is illustrated by comparison to the experimentally observed ME in [20]. The journal $\Delta\Delta T$ is the root cause of the ME simulation, and it is heavily influenced by the fluid-film leading-edge temperature distribution. Thus, applying the 2D-MC-deep learning approach has great potential for improving the accuracy of ME simulations.

2. Modeling methodology

2.1. Rotor-bearing model

Fig. 2 shows the entire computational domains [20] for the ME simulation, including the rotor-bearing system. The rotor with the overhung mass is supported by linear and non-linear TPJBs with five pads. The linear bearing is modeled with conventional stiffness and damping coefficients in the rotordynamic model (elastic rotor domain). The non-linear TPJB is modeled with a 3D TEHD (Thermo-Elasto-Hydro-Dynamic) model. The computational domains of the TPJB model consist of the fluid-film and pad domains. The flow model for the fluid-film domain is represented by the generalized Reynolds equation, which accounts for 3D viscosity variation in the fluid film. The generalized Reynolds equation can be derived from the continuity and momentum equations with the suitable assumptions (laminar, incompressible, no inertia effect, no journal curvature effect, etc.) [21].

Fluid-film flow model. Generalized Reynolds Equation (p, fluid-film domain):

$$\nabla \cdot (D_1 \nabla p) + (\nabla D_2) \cdot U_s + \frac{\partial h_l}{\partial t} = 0 \tag{2}$$

where p is the static pressure, U_s is the journal rotating surface velocity, and D_1 and D_2 are.

$$D_1 = \int_0^{h_l}\int_0^z \frac{\xi}{\mu_l} d\xi dz - \int_0^{h_l}\frac{\xi}{\mu_l}d\xi \int_0^{h_l}\int_0^z \frac{1}{\mu_l} d\xi dz \;/\; \int_0^{h_l}\frac{1}{\mu_l}d\xi \tag{3}$$

$$D_2 = \int_0^{h_l}\int_0^z \frac{1}{\mu_l} d\xi dz \;/\; \int_0^{h_l}\frac{1}{\mu_l}d\xi \tag{4}$$

where μ_l is the fluid's dynamic viscosity. The film thickness (h_l) between the journal and pad surfaces can be written as.

$$h_l = C_{l,p} - \{x_R + z\theta_{Ry} - x_{pvt}\cos(\theta_p) - \alpha_{pit}\cos(\theta_p)\}\cos(\theta) - \{y_R - z\theta_{Rx} - x_{pvt}\sin(\theta_p) - \alpha_{pit}\sin(\theta_p)\}\sin(\theta) - (C_{l,p} - C_{l,b})\cos(\theta - \theta_p) - \delta_{tlt}R_s\sin(\theta - \theta_p) - h_{j,TE} - h_{p,TE} \tag{5}$$

REF _Ref81801295 \h Fig. 3(a) depicts the film thickness parameters, and the rotor and pad degrees of freedom (dofs) are illustrated in Fig. 3(b)–(d). The TPJB design parameters R_s, $C_{l,b}$, $C_{l,p}$, and θ_p are the journal radius, radial bearing clearance, radial pad clearance and pad angular position. The variables x_R and y_R are the journal center position coordinates, x_{pvt} is the pad pivot deformation, δ_{tlt} (tilting) and α_{pit} (pitch) are the pad angular motion coordinates, θ_{Rx} (pitch) and θ_{Ry} (yaw) are the journal angular motion coordinates, $h_{j,TE}$ and $h_{p,TE}$ are the film thickness changes caused by the journal and pad thermal deformation, and θ and z are the angular and axial positions in the global coordinate.

The boundary conditions for the generalized Reynolds equation include zero pressure at both sides of the fluid-film, and pressures at the trailing and leading edges imposed by the artificial neural network [18].

The fluid dynamic viscosity varies with temperature as ($\mu_l = \mu_o e^{(\alpha(T_l - T_o)}$ where μ_o: reference dynamic viscosity, α: viscosity coefficient, T_o: reference temperature, and the lubricant temperature (T_l) is obtained from solution of the energy equation:

Fluid-film thermal model (T_l, fluid-film domain):

$$\rho_l c_{p,\,l}\left(\frac{\partial T_l}{\partial t} + \vec{U}\cdot\nabla T_l\right) = \nabla\cdot(\lambda_l \nabla T_l) + \mu_l\left[\left(\frac{\partial u}{\partial y}\right)^2 + \left(\frac{\partial w}{\partial y}\right)^2\right] \tag{6}$$

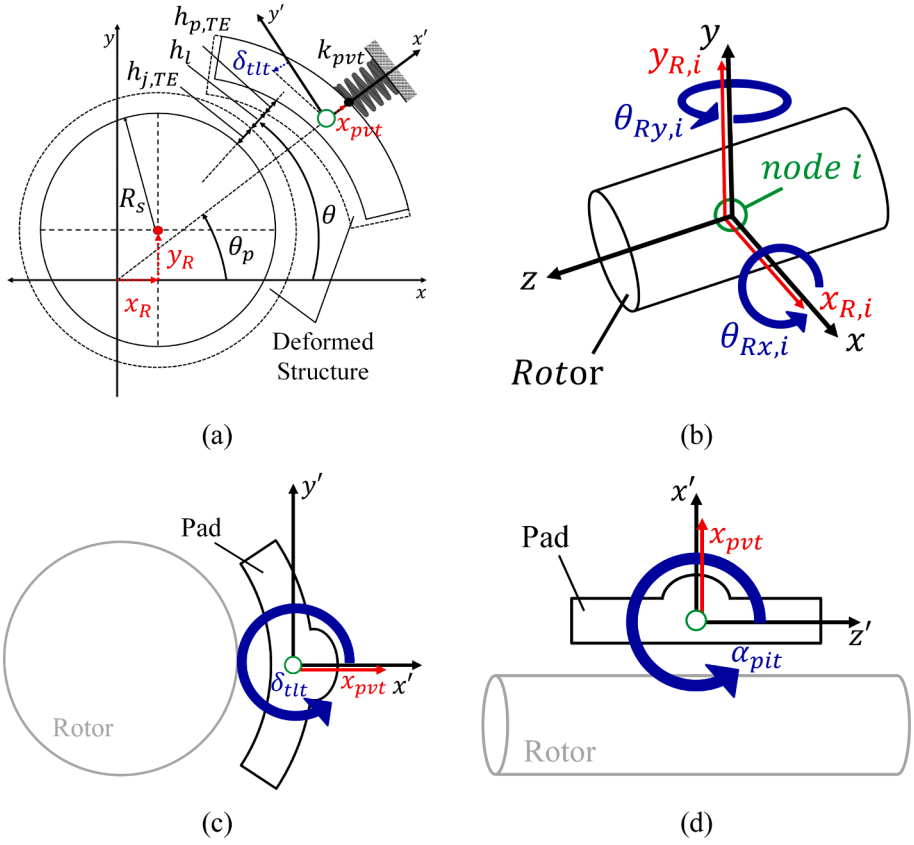

Fig. 3. Film thickness parameters and dofs for structure model; (a) film thickness parameters, (b) rotor dofs, (c) x'-y' (local coordinate) view pad dofs, (d) z'-x' (local coordinate) view pad dofs.

where ρ_l, $c_{p,l}$, and λ_l are the fluid density, specific heat, and thermal conductivity, respectively, $\vec{U}$ is the fluid velocity vector with components u, v, w, and the velocity field can be acquired from the pressure solution in Eq. (2) [9]. A zero gradient temperature is applied to the trailing-edge and axial ends of the fluid-film, and both axial ends of the fluid-film are prescribed as ambient temperature if reverse flow occurs. The temperature at the fluid-film leading-edge is determined by the 2D-MC discussed in Section 2.2. Heat flux continuity is imposed at the interfaces between the fluid-film and pad (or journal) [16]. The FVM (Finite Volume Method) is employed to solve the governing equations for the fluid-film domain, with local conservation of mass and energy [16–17], and the FEM (Finite Element Method) is employed for structural modeling.

A structure-thermal model for the thermal rotor and pad domains is included to determine their temperature distributions (T_s). The governing equation for transient heat conduction is:

Structure thermal model (T_s, thermal rotor and pad domains):

$$\rho_s c_{p,\,s}\frac{\partial T_s}{\partial t} = \nabla\cdot(\lambda_{\,s}\nabla T_s) \tag{7}$$

where ρ_s, $c_{p,s}$, and λ_s are the solid density, specific heat, and thermal conductivity, respectively. The thermal boundary conditions, except for the interfaces between the solid and fluid-film domains, are prescribed by a heat convection coefficient and the ambient temperature. While a zero-gradient is imposed on the fluid-film's trailing edge as the thermal boundary condition, in the case of the pad's trailing edge, the heat transfer coefficient and ambient temperature are prescribed. Thermal deformation of the pads and rotor are calculated utilizing the temperature solution in the solid domains, yielding the total displacement solution. Refer to [9,16] for detailed information on the mechanical structure model. Film thickness changes ($h_{j,TE}$, $h_{p,TE}$) resulting from structural thermal deformation, thermal imbalance ($e_{bw,i}$) and thermal bow (magnitudes ($\theta_{bw,i}$) and phase angles ($\varphi_{bw,i}$, $\psi_{bw,i}$)) can be evaluated from the total displacement solution [17]. The term "thermal bow" refers to the thermally induced bow amplitude and phase angle of the rotor which acts as an imbalance-like source, unless indicated otherwise in the paper.

The rotordynamic model provides the rotor's total displacement vector $\{x_t\}$ vs time with 4 dofs (right-hand rule) $\left\{x_{R,i}, y_{R,i}, \theta_{Rx,i}, \theta_{Ry,i}\right\}$ per rotor node, as represented in Fig. 3(b). The rotor displacements are obtained by solving through Eqs. (8)–(12), where the subscript i indicates the value for node i.

Rotordynamic model ($\{x_r\}$, elastic rotor domain):

$$\begin{aligned}[M_R]\left\{\ddot{x}_r\right\} + \left([C_R] + [C_{gs}] + [C_{lb}]\right)\left\{\dot{x}_r\right\} + \left([K_R] + [K_{lb}]\right)\{x_r\} \\ = \{F_{im}\} + \{F_{nb}\} + \{F_{bw}\}\end{aligned} \tag{8}$$

$[M_R]$ and $[K_R]$ are the elastic rotor mass and stiffness matrices [17], respectively, $\{x_r\}$ is the relative displacement, and $\{F_{im,i}\}$, $\{F_{nb,i}\}$, and $\{F_{bw,i}\}$ are mechanical imbalance, non-linear bearing, and thermal bow force vectors. The force vectors are given by Eqs. (9)–(11).

$$\left\{F_{im,i}\right\} = \left\{m_{im,i}e_{im,i}\omega_R^2\cos\left(\omega_R t + \varphi_{im,i}\right),\;\; m_{im,i}e_{im,i}\omega_R^2\sin\left(\omega_R t + \varphi_{im,i}\right),\;\; 0,\;\; 0\right\}^T \tag{9}$$

$$\left\{F_{nb,\,i}\right\} = \left\{F_{fx,\,i},\;\; F_{fy,\,i},\;\; 0,\;\; 0\right\}^T \tag{10}$$

$$\left\{F_{bw,\,i}\right\} = \begin{Bmatrix} m_{R,i}\; e_{bw,\,i}\;\omega_R^2\cos\left(\omega_R t + \varphi_{bw,\,i}\right) \\ m_{R,i}\; e_{bw,\,i}\;\omega_R^2\sin\left(\omega_R t + \varphi_{bw,\,i}\right) \\ -I_{T,\,i}\;\theta_{bw,\,i}\;\omega_R^2\sin\left(\omega_R t + \psi_{bw,\,i}\right) \\ I_{T,\,i}\;\theta_{bw,\,i}\;\omega_R^2\cos\left(\omega_R t + \psi_{bw,\,i}\right) \end{Bmatrix} \tag{11}$$

$$\{x_t\} = \{x_r\} + \{x_{bw}\} \tag{12}$$

$[C_{gs}]$, $[C_{lb}]$, and $[K_{lb}]$ are the gyroscopic damping, linear bearing damping, and linear bearing stiffness matrices [17], m_{im} is the mechanical (initial) imbalance weight, $e_{im,i}$ and $\varphi_{im,i}$ are the mechanical imbalance magnitude and phase angle, $F_{fx,i}$ and $F_{fy,i}$ are the non-linear bearing fluidic × and y direction forces, $m_{R,i}$ and $I_{T,i}$ are the rotor mass and transverse mass moment of inertia, and ω_R is the rotor spin frequency.

The rotordynamic model interacts with the fluid-film and rotor deformation models. The pressure solution (p) in Eq. (2) of the fluid-film model is applied to the rotordynamic model as the fluidic forces ($F_{fx,i}$, $F_{fy,i}$) of Eq. (10). The film thickness in the fluid-film model (Eq. (5)) is influenced by the total displacement solution $\{x_t\}$ (Eq. (12)) at the non-linear bearing node. Also, the thermal imbalance and bow with its phase angles in Eq. (11) are determined by the rotor deformation model [17]. In addition, the pad dynamic model is considered with the rigid pad assumption, and the dynamic equations for the rigid pad can be expressed by Eqs. (13) and (14), where only the tilt angle is considered and pitch is neglected.

Pad dynamic model (x_{pvt}, δ_{tlt}; rigid pad):

$$M_{PG}\,\ddot{x}_{pvt} + k_{pvt}\,x_{pvt} = \sum_i\left(F_{n,\,i} + F_{t,\,i}\right) \tag{13}$$

$$I_G\,\ddot{\delta}_{tlt} = \sum_i \left(M_{n,i} + M_{t,i}\right) \tag{14}$$

where M_{PG} and I_G are the pad mass and pad moment of inertia. $F_{nx,i}$ and $F_{tx,i}$ are the pivot direction forces from the normal and tangential fluid forces on the pad surface, and the fluid forces determine the moments $M_{n,i}$, and $M_{t,i}$. The fluidic forces and moments on the pad are calculated by the fluid-film pressure solution, and the pad dynamic model's solution (x_{pvt}, δ_{tlt}) updates the film thickness during the simulation.

2.2. Deep learning 2D-MC application

As described in Section 2.1, the fluid-film leading-edge temperature is prescribed by the artificial neural network, trained via CFD-generated data. The CFD provides more reliable results for the groove thermal-flow as compared with utilizing conventional constant-MC approaches. Applying CFD to the groove model directly would be computation time impractical, especially considering the 3D, multiphysics, nonlinear, transient, large order, wide ranging time constant nature of the ME. A practical implementation of the CFD groove model is enabled by using the artificial neural network ANN as a surrogate groove, after training the neural network based on CFD results. The accuracy of the ANN approach is benchmarked against a full CFD model of the groove.

In [19] Yang and Palazzolo introduced a deep convolutional autoencoder neural network as the surrogate groove model based on excellent performance related to the image-to-image prediction [22]. The excellent image prediction supported the capability for the 2D-MC. Trained artificial neural networks provided high accuracy for various oil injection types, when utilized for TPJB static performance prediction. The pre-trained neural networks for the oil injection types are implemented here for ME simulation. The CFD model verified in the prior research [19] is also applied. This utilizes the Reynolds-Averaged-Navier-Stokes (RANS) equation, with thermal, transitional turbulence (k-w SST (Shear Stress Transport), gamma transitional), and cavitation effects are adaptably implemented [19]. The fluid energy equation includes the viscous dissipation term [21], and the detailed model descriptions are available in Ref. [18].

The overall schematic for prescribing the fluid-film leading-edge temperature in the ME simulation is illustrated in Fig. 4. The groove thermal-flow is simulated with CFD for a massive input set. The input set is generated based on the DOE (Design of Experiment) method [18], and the details for the input parameters and its ranges are given in Section 3.1. The 2D-MC data from the CFD simulations are used to train the deep convolutional autoencoder neural network, and the trained neural network has the ability to predict the 2D-MC with respect to the various groove geometric and operating parameters. The 2D-MC (η_{2D}) from the trained neural network is substituted into the non-dimensional temperature (η) at pad leading-edge of the fluid-film, to obtain the 2D temperature distribution (T_{out}) in the ME solver as.

$$\eta(r,z) \equiv \frac{T_{out}(r,z) - T_{sup}}{T_{in} - T_{sup}} = \eta_{2D}(r,z) \tag{15}$$

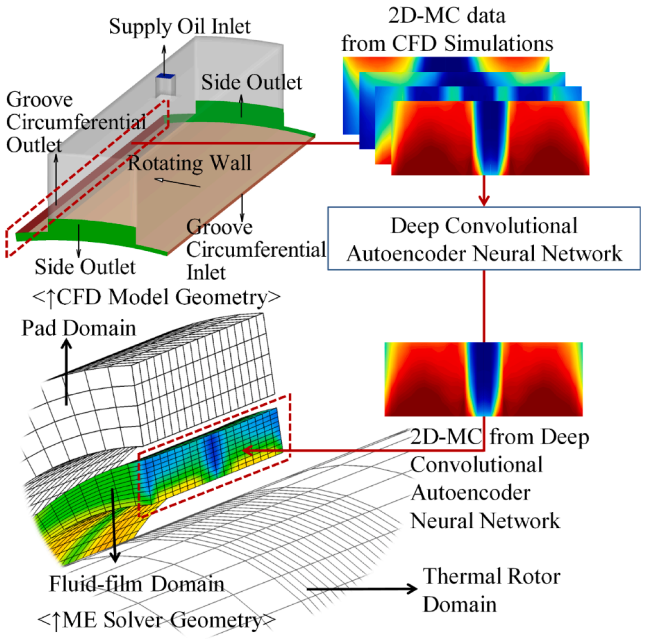

Fig. 4. Overall Schematics for fluid-film leading-edge temperature prescription.

2.3. Calculation procedure

Fig. 5 represents the suggested ME algorithm to implement the 2D-MC approach. The staggered time integration scheme [9,11,17] provides efficient computation for the ME simulation, which has a large time-scale disparity between the structure dynamic and structure thermal responses. There are two time-scales which are defined as the short (local, Δt_l) and long (global, Δt_g) time-scales. The short time-scale has the order of the shaft rotation, and the long time-scale is empirically selected as two-hundred shaft rotation periods. As seen in Fig. 5, there exists time integration solvers with each time-scale, and that is sequentially and iteratively implemented until the ME solver reaches the user-input total time (t_{stop}).

The rotor and pad dynamic models are coupled with the fluid-film flow and thermal models and 2D-MC model, and are solved with an adaptive Runge-Kutta (adaptive time step, Δt) algorithm for the short time-scale integration. The dependent variables are updated in each solver, while transferring and updating the variables between component solutions, during the short time-scale integration. The displacement and velocity solutions in the rotor and pad dynamic models update the film thickness and its derivatives in the fluid-film model, and the pressure solution in the fluid-film flow model transfers the new fluidic forces to the rotor and pad dynamic models. The 2D-MC model continues to update the fluid-film leading-edge temperature according to the given operating conditions. The fluid-film flow and thermal models are coupled via the velocity field obtained from the pressure solution, and dynamic viscosity obtained from the fluid temperature solution.

The long time-scale time integration solver starts after executing the short time-scale integration, including the condition for vibration orbit convergence. The former provides the time-varying structure temperature and total displacement during the global time step, utilizing the structure thermal and deformation models. The thermal interface boundaries between the structure and fluid-film models are updated continuously, and the temperature solution is transferred to the interface boundaries of the fluid-film thermal model. In addition, the total displacement solution from the thermal deformation model is used to evaluate the thermally induced, rotor mass imbalance and bow (synchronous force sources) in the rotordynamic model, and the film thickness changes due to thermal deformation.

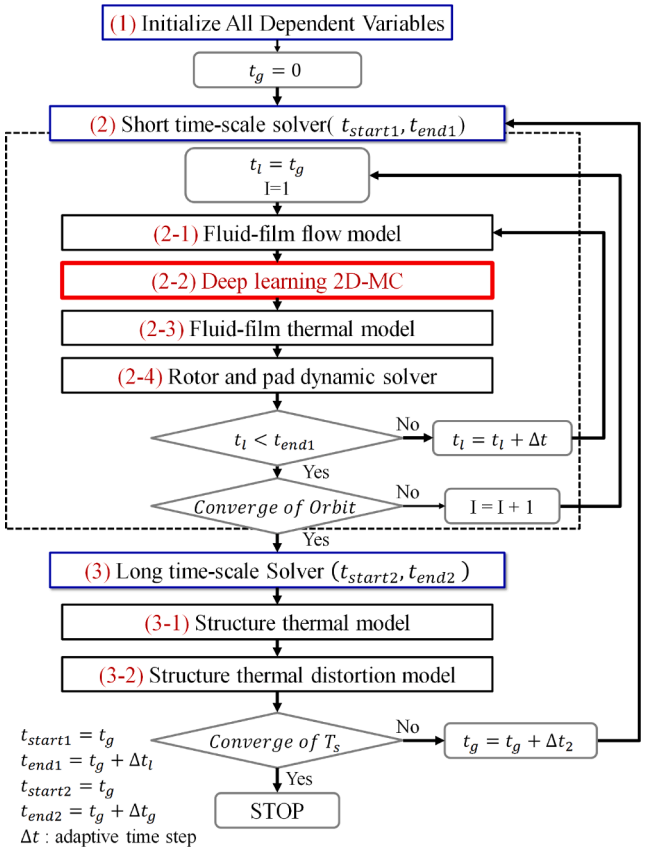

Fig. 5. ME dynamic simulation algorithm considering 2D-MC.

3. Results and discussion

3.1. Case and dataset

The rotor-bearing system for ME simulation is illustrated in Fig. 2. The rotor holds a large overhung mass at the right rotor-end, and the rotor is supported by the linear and non-linear bearings. The linear bearing is modeled by the isotropic stiffness (170 MN/m) and damping (100 kN•s/m) coefficients. The time-varying force on the rotor from the non-linear bearing is calculated via the bearing model described in Section 2. The specific input parameters are provided in Table 1. In addition to the parameters in Table 1, the pad thickness, pad arc length, and pad offset are 12.7 mm (15 mm at pivot), 15 mm, and 0.5, respectively. The 3 lubrication states considered are direct (small nozzles with open end seals), flooded (large orifices with closed end or very small clearance seals) and mixed (closed end or small clearance seals, with small orifices or nozzles).

The four oil injection types considered for the TPJB include:

(1) Case-A: 1 small orifice ($D_g/W_g = 0.169$), closed-end seal, in Fig. 6(a), (mixed)
(2) Case-B: 1 large orifice ($D_g/W_g = 0.357$), closed-end seal, in Fig. 6(a), (flooded)
(3) Case-C: 1 nozzle ($D_g/W_g = 0.282$), open-end seal, in Fig. 6(b), (direct)
(4) Case-D: 3 nozzles ($D_g/W_g = 0.171$), open-end seal, in Fig. 6(c), (direct)

Yang and Palazzolo [19] presented a 2D-MC model for the above oil injection types as the surrogate groove model. The researchers employed the convolutional autoencoder neural networks to train the 2D-MC via CFD-informed data, including 1,536 training data and 658 test data for each oil injection type. The design space on the training data was obtained utilizing a hybrid DOE method [18] with the full factorial and Latin Hypercube Sampling (LHS) method, and the test data was extracted by random input parameter combinations. The trained neural networks for the oil injection types showed superior neural network performance (see RMSE and R-squared in Table 2), and are adopted in this ME study. The detailed groove parameters, parameter range for the DOE, and pre-trained neural network performance are given in Table 2.

The high effectiveness of the pre-trained neural networks is also verified through comparison of the half-symmetric, 2D-MC contours at the fluid-film leading-edge, as shown in Fig. 7. The left figures in Fig. 7 (1) represent the MC contour predicted by the CFD, and the right figures in Fig. 7 (2) are obtained from the pre-trained neural networks. A large number of contours are shown corresponding to randomly extracted test data to demonstrate generality of the agreement. The 2D-MC pre-trained neural network approach also shows excellent agreement with the original CFD data for all oil injection types.

3.2. Model validity

As described in Section 2, the theoretical model for the TPJB consists of fluid and dynamic structure sub-models. The fluid model involves the fluid-film and groove models. The groove model's simplification in the conventional Reynolds approach invokes motivation to develop a full CFD model (based on solving the full Navier-Stokes equations). Recent studies [21,23] presented CFD TPJB models with verification. However, the Reynolds approach is still needed because of the intense computational load of CFD. Direct application of CFD in the TPJB model as applied with ME simulation is clearly infeasible since this involves a large order structural model, nonlinearities, and numerical integration of a system with both short and long time scales (time constants).

In [19] Yang and Palazzolo improved the Reynolds-based TPJB model by combining it with the deep learning 2D-MC model for the static and dynamic coefficient prediction, and they showed the model validity via comparison with verified CFD results [23]. Even though the model verification was performed only for obtaining static response and dynamic coefficient prediction, the model validity is still effective in the ME simulation since both models share identical fluid-film models.

In addition, the ME simulation results in this study are compared to test data [20] and prior studies [11,17] as a validity check. Table 3 represents the ME occurrence speed ranges observed in the experiment and simulations. Tong and Palazzolo [11] utilized a 3D

Table 1
Input parameters for ME simulation [17].

Parameters	Value
Shaft diameter [mm]	101.6
Bearing length [mm]	50.8
Bearing radial clearance [mm]	0.0749
Preload	0.5
Pivot type	Spherical
Load type	Load On pad (LOP)
Outside H.C.C. [W/m^{2}K]	50 (Shaft), 500 (Pad)
Ambient temperature [C]	30 (Shaft), 55 (Pad)
Supply oil temperature [C]	50
Lubricant	ISO 32
Material (solid domains)	Steel

* H.C.C.: Heat convection coefficient.

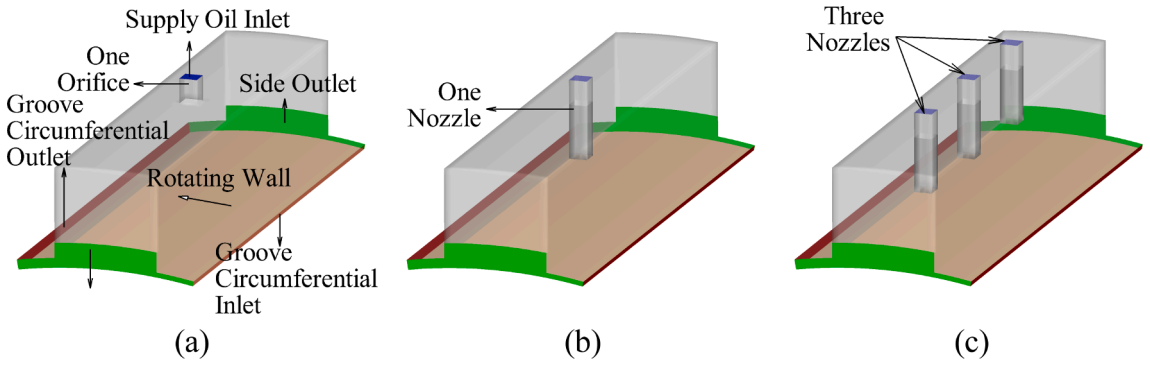

Fig. 6. Oil injection type geometries; (a) one orifice, (b) one nozzle, (c) three nozzles.

Table 2
DOE design space and performance on deep convolutional autoencoder neural networks [19].

Oil injection type	Case 1	Case 2	Case 3	Case 4
Constant input parameters				
D_g/W_g	0.169	0.357	0.282	0.171
h_s/R_s	0.0084	0.0063	0.0500	0.0500
$C_{l,b}/R_s$	0.0015	0.0015	0.0015	0.0015
Pre-trained neural network input parameters and their ranges				
R_s [mm]	25.4 – 76.2			
L_b/R_s	0.4 – 1.0			
U_s [m/s]	15 – 95			
P_t [MPag]	0.01–0.70			
P_{in} [MPag]	0 – 1.2			
P_{out} [MPag]	0 – 0.65			
$h_{in}/C_{l,b}$	0.3 – 2.2			
$h_{out}/C_{l,b}$	0.3 – 2.2			
T_{in} [C]	50 – 120			
			Performance of pre-trained neural networks	
R-squared (train data)	0.995	0.997	0.996	0.997
RMSE (train data)	0.025	0.023	0.020	0.019
R-squared (test data)	0.987	0.988	0.985	0.992
RMSE (test data)	0.041	0.043	0.039	0.029

* Refer to nomenclature for parameter description above.

TEHD model with the constant-MC model to impose the fluid-film leading-edge temperature. The predicted ME speed range was narrower than experimentally measured. Yang and Palazzolo [17] further advanced the ME model by including an axially varying MC (1D-MC) acquired from CFD-informed machine learning. The ME occurrence speed range prediction accuracy improved relative to the previous study [11] and experiment. The present ME model includes radially and axially varying MC effect (2D-MC), obtained through CFD and deep learning, and the ME occurrence speed range in the simulation corresponds well with experimental observation. These comparisons were made to establish the validity of the present approach, prior to parameter variation studies.

The model predictions are compared to additional experimental data available in the literature [24,25] for further validation. Table 4 shows the input data for these check cases, labeled as Case-(1) and Case-(2). In Case-(1), Hagemann et al. [24] measured pad temperatures for a leading edge groove LEG type TPJB under static loading. The journal and pad degree of freedom (dof) motions are iteratively solved until force equilibrium is obtained [16]. The CNN of the Case-C oil injection described in Section 3.1, and the 2D-MC for the LEG type in Case-(1) is employed from the CNN obtained in Ref. [19]. Fig. 8 shows good agreement between the simulation results and measurements for the pad temperature. Most notably, the peak pad temperature recorded at the sensor with the maximum temperature shows good agreement between theory and test, for all operating speeds.

In Case-(2), Tong et al. [25] spun an eccentrically machined rotor with a 3 nozzle fed TPJB to replicate the synchronous journal motion during a ME. The journal ΔT's were measured with RTDs implanted around the circumference of the journal and with a slip ring. Constant circular motion of the journal is assumed and the pad dof motions are solved. The simulation and test data [25] for the synchronous circular orbit condition are compared in Fig. 9. The 2D-MC based predictions show good agreement with measurement, while the conventional constant MC (1.0, 0.4) based predictions (Eq. (16)) are widely different from each other and the measurements.

Summarizing, these results indicate using the conventional MC approach yields widely varying temperature predictions depending on the choice of MC, and in contrast the 2D-MC approach yields accurate predictions relative to measurements.

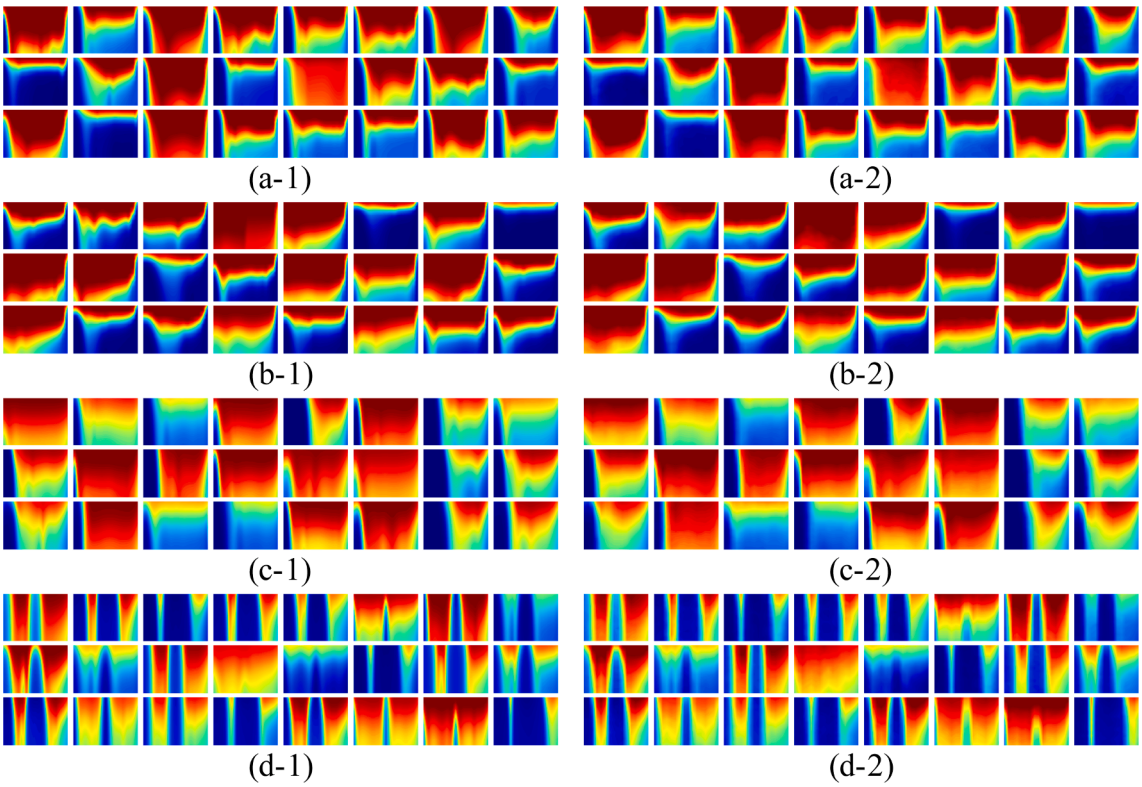

Fig. 7. 2D-MC comparison between CFD and deep learning for random test data; (1) CFD, (2) Deep Learning, (a) Case-A, (b) Case-B, (c) Case-C, (d) Case-D; *Left: x-y symmetry line, Top: journal surface, Bottom: pad surface, Right: side outlet, Contour color (rainbow): red = 1.0, blue = 0.0.

Table 3
Model validity investigation.

Researchers	Method	Main features	Observed ME speed range [RPM]
De Jongh et al. [20]	experiment	–	7,200 – 9,400
Tong et al. [11]	simulation	constant-MC	7,000 – 8,000
Yang et al. [17]	simulation	1D-MC ANN	8,000 – 9,200
Present	simulation	2D-MC ANN	7,500 – 9,500

Table 4
Input data from the literature for further model validation.

	Case-(1)	Case-(2)
Researchers	Hagemann et al. [24]	Tong et al. [25]
Load condition	Static load, 17.3 kN	Synchronous circular orbit with 68.6 um radius and 0 eccentricity
Load type	Load between Pads (LBP)	Load on Pad (LOP)
Oil injection type	LEG	Three-nozzles
Lubricant type	ISO 32	ISO 46
Supply temperature [C]	50	28 (cool), 41 (hot)
Pad number	4	5
Pad preload	0.5	0.42
Pad arc length [deg]	70	56
Bearing Length [mm]	72	80
Journal radius [mm]	60	40
Radial clearance [um]	108	140
Pivot offset [%]	60	50
Operating speed [RPM]	4,000 – 15,000	1,000 – 5,500

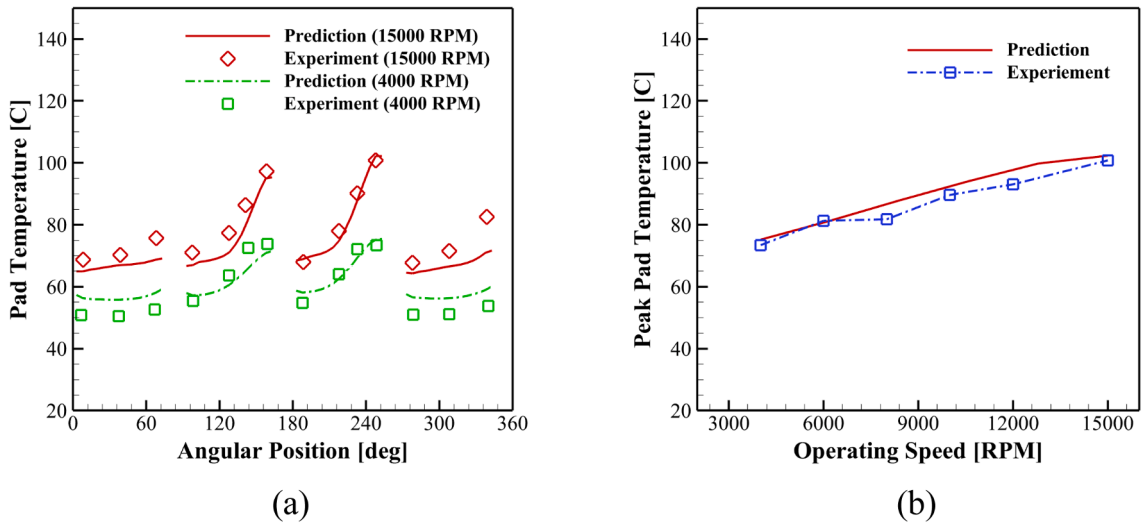

Fig. 8. Comparison between prediction and experiment [24] for a LEG type bearing (Static load condition); (a) Pad temperature distribution, (b) Peak pad temperature; *2D-MC obtained from LEG type injection [19].

3.3. ME simulation

The dynamic simulation of the rotordynamic system results are discussed in this section. The initial temperature of the solid domain is 40 degC, and the initial rotor position normalized by the radial bearing clearance ($x/C_{l,b}$, $y/C_{l,b}$) is 0 in the x-direction and −0.2 in the y-direction. The dynamic simulation is executed for 20 min, while maintaining a constant operating speed and supply oil flowrate of 15 LPM. The simulation time is 9,310 s for each case, when utilizing a single core of Intel Xeon CPU E5-1650 v4 3.6 GHz. The rotor system model is obtained from references [10,11], and [20], the latter providing experimental results and test rotor description. The specific rotor input is presented in Tables 6 and 7.

3.3.1. Constant-MC and 2D-MC comparison

The importance of the 2D-MC model is highlighted from the results in Figs. 10–12. These results correspond to the injection type Case A (1 small orifice, closed-end seal, in Fig. 6(a)). The conventional constant-MC approach does not provide a 2D fluid-film leading-edge temperature distribution, while the 2D-MC approach does provide the more realistic 2D distribution. This may have a significant influence on the journal temperature for the ME. The constant-MC approach employed in this research can be mathematically written as.

$$\eta(r,z) = \min[Q_{in}/Q_{out}, \eta_k] \tag{16}$$

where Q_{in} and Q_{out} are the groove circumferential inlet and outlet flowrates, and η_k is the constant-MC. The choice between MC models may have a large effect on the predicted ME. Constant MC-model values of 0.4, 0.6, 0.8, and 1.0 are considered for comparison with the proposed 2D-MC approach. Simulations that include the ME are labeled as "w/ ME", which implies that the thermal bow force vector is included in the rotordynamic model. Simulations that exclude the ME are labeled as "w/o ME", which implies that the thermal bow force vector is not included in the rotordynamic model. The "w/o ME" results are presented for comparison to clearly identify cases that have a ME synchronous vibration instability. The system is considered to be experiencing the ME if the vibration and ΔT in the "w/ ME" results are much larger than that in the "w/o ME" case.

Fig. 10 shows the predicted dynamic simulation results including the peak-to-peak amplitude at the bearing location and ΔT. The numerical integration based results, including vibration amplitude and journal ΔT, typically oscillate with time, reach steady-state or encounter a near rub condition which terminates the simulation. The responses are presented in the following formats: (1) averaged value for the last 2 min if near rub does not occur, and (2) immediate value if near rub occurs. Near rub occurs when the normalized minimum film thickness ($h_{min}/C_{l,b}$) drops below 0.1, at which time the simulation is terminated. Figs. 10–12 correspond to the injection type Case A (1 small orifice, closed-end seal, in Fig. 6(a)). The legend"2D-MC" indicates that the 2D MC results are utilized in the model.

A ME event occurs when the vibration and ΔT are much larger than the "w/o ME" results. The ME in the experiment [20] was observed at operating speeds from 7,500 RPM to 9,400 RPM. The simulation results considering the 2D-MC and 0.4, 0.6-MC have good agreement with the experimental data, while the results by 0.8, 1.0-MC do not indicate a ME event. This indicates that ME simulation results depend strongly on the value selected for the constant-MC. However, the MC is in practice typically guessed based on experience, and may be a strong function of groove geometry and operating parameters. This is a major drawback of the constant-MC approach, and the results in Fig. 10 suggest the advantage/benefit of the proposed 2D-MC approach.

Fig. 11 shows "w/o ME" results for the constant-MC and 2D-MC models, for later comparison with the "w/ ME" results. Steady state

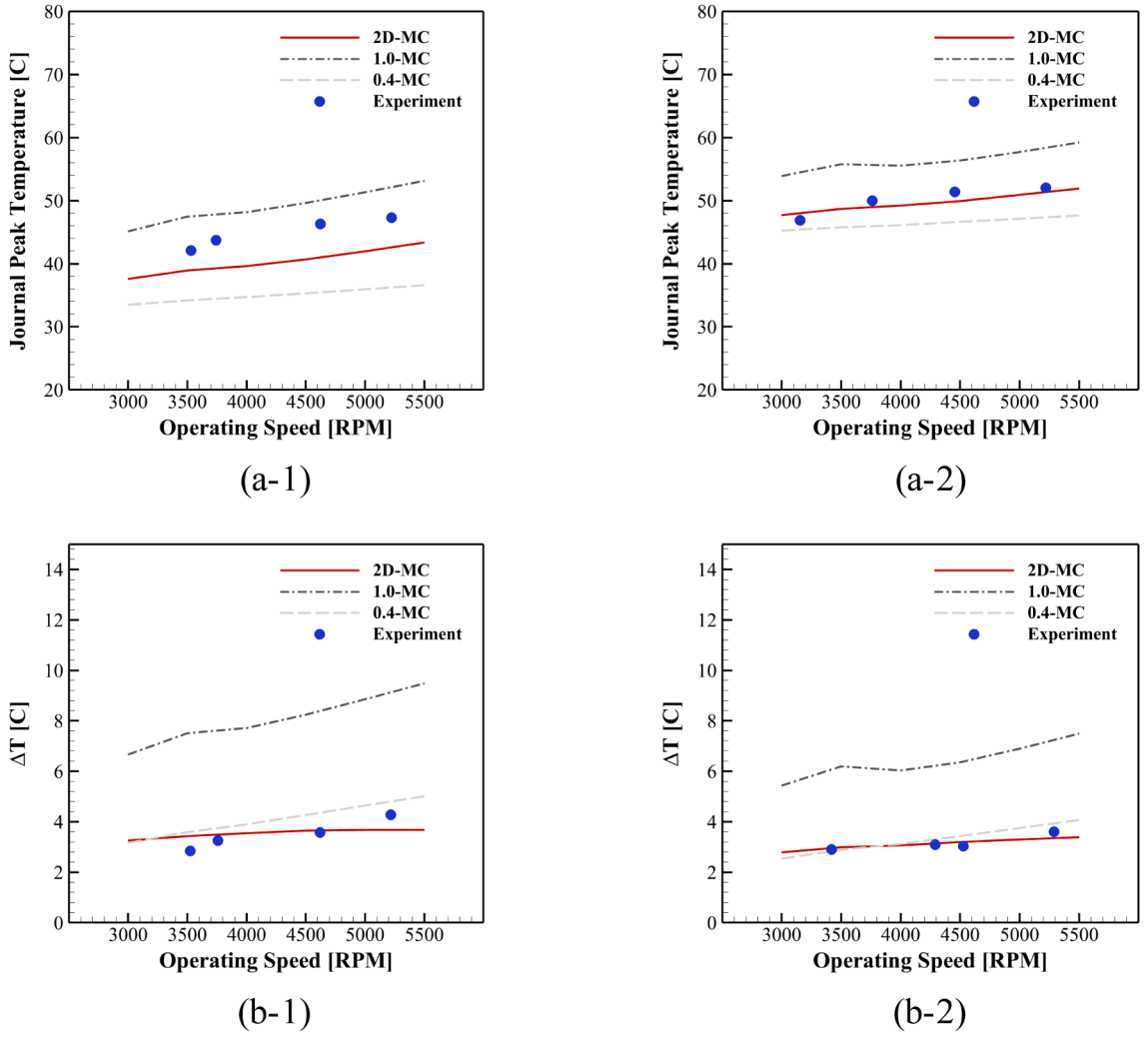

Fig. 9. Comparison between prediction and experiment [25] for a three-nozzle type bearing with a synchronous circular orbit condition; (1) Cool-oil condition, (2) Hot-oil condition, (a) Journal peak temperature [C], and (b) ΔT [C]; *2D-MC obtained from Case-C injection.

Table 6
Rotor node information.

Total node number	20
Total element number	19
Applied mass imbalance node	18
Applied mass imbalance magnitude [kgm]	2.74E-04
Applied mass imbalance phase angle [deg]	0

values are presented and obtained from long duration runs of transient simulations. As represented in Fig. 11(a) and Fig. 11(b), the vibration magnitude and ΔT peak near 7,500 RPM, for all MC models. For large vibration conditions, the journal experiences thinner min film thickness (higher max heat dissipation) and thicker max film thickness (lower min heat dissipation) during whirling orbit motions. Thus, the large vibration may cause significant journal ΔT. The thermal bow angle is shown in Fig. 11(d). Thermal bow is omitted as a forcing source in the "w/o ME" results but can still be calculated from the journal temperature distribution and displayed as in Fig. 11(d).

A comparison of Figs. 10 and 11 shows a seemingly contradictory result. The Morton effect occurs for the low constant MC cases (0.4, 0.6) and does not occur for the high constant MC cases (0.8, 1.0) in Fig. 10, even though the low constant MC cases exhibit lower vibration amplitude and ΔT than the high constant MC cases for the "w/o ME" results in Fig. 11. This contradiction may be resolved by considering the thermal bow influenced hot spot, and heavy spot angles for these cases. The heavy spot (applied mechanical

Table 7
Rotor element lengths and diameters.

Element No.	Length [m]	Diameter [m]
1	0.027	0.198
2	0.078	0.114
3	0.054	0.082
4	0.069	0.082
5	0.069	0.082
6	0.041	0.122
7	0.071	0.357
8	0.149	0.122
9	0.124	0.184
10	0.124	0.184
11	0.047	0.102
12	0.043	0.102
13	0.109	0.093
14	0.085	0.082
15	0.013	0.113
16	0.019	0.507
17	0.019	0.507
18	0.019	0.434
19	0.033	0.198

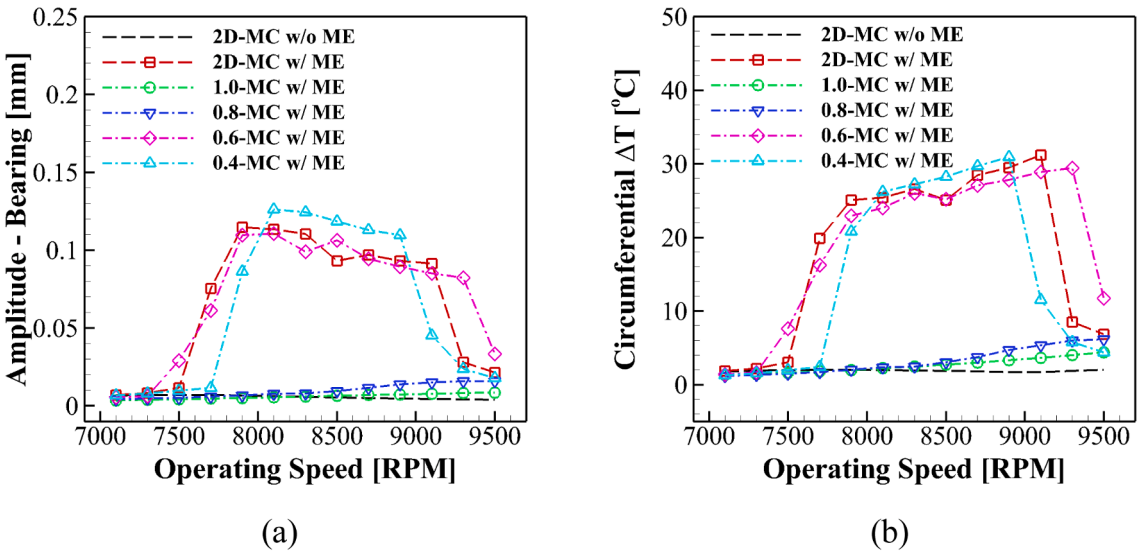

Fig. 10. Dynamic simulation results; (a) amplitude at bearing (1x, peak-to-peak), (b).ΔT.

imbalance) is located at 0 deg, and the heavy spot leads the high spot (min film thickness). The hot spot (max journal temperature angle) lags behind the high spot. The thermal bow has an approximately 180 deg difference from the hot spot. Amplification of the vibration occurs as the thermal bow and heavy spot coincide, which is a cause of the ME. As seen in Fig. 11(c) for the "w/o ME" case, all high spots follow the heavy spot with similar differences, while the thermal bow in Fig. 11(d) differs according to the constant-MC or 2D-MC model. As an approximation the thermal bow vector is directed 180 deg opposite the hot spot, thus Fig. 11(d) implies that the predicted hot spot location varies widely according to which MC model is employed. Fig. 9(d) shows that the low constant-MCs and 2D-MC are closer to the heavy spot than the high constant-MCs. Here, the closer coincidence of the thermal bow and heavy spot spawn the ME in the low constant-MCs and 2D-MC. These results also imply that the hotspot location is strongly dependent on the choice of constant MC value, even to the point of predicting or not predicting an ME event. The risk of course is missing predicting an ME event when it will actually occur in the machine.

An intuitive interpretation of the between pad mixing with supply oil would identify the following features of the leading-edge film temperature; (a) low temperature is formed near the oil injection and side outlet due to the considerable mixing of the supplied and discharged oil, and (b) the shaft surface is hotter than the pad surface [16]. These are confirmed by the temperature plot for the 2D-MC model in Fig. 12(a), but are noticeably absent in the plot for the constant (0.4) MC case in Fig. 12(b). The 2D-MC and 0.4-MC show similar the dynamic simulation results "w/o ME" in Fig. 11. This demonstrates that the high-fidelity 2D-MC model's accuracy can be achieved utilizing a constant-MC, if a suitable MC is selected. However, this does not guarantee that the agreement will also occur for the "w/ ME" simulation, and Fig. 10 shows that there is still a large disparity between the 2D-MC and constant (0.4) MC models.

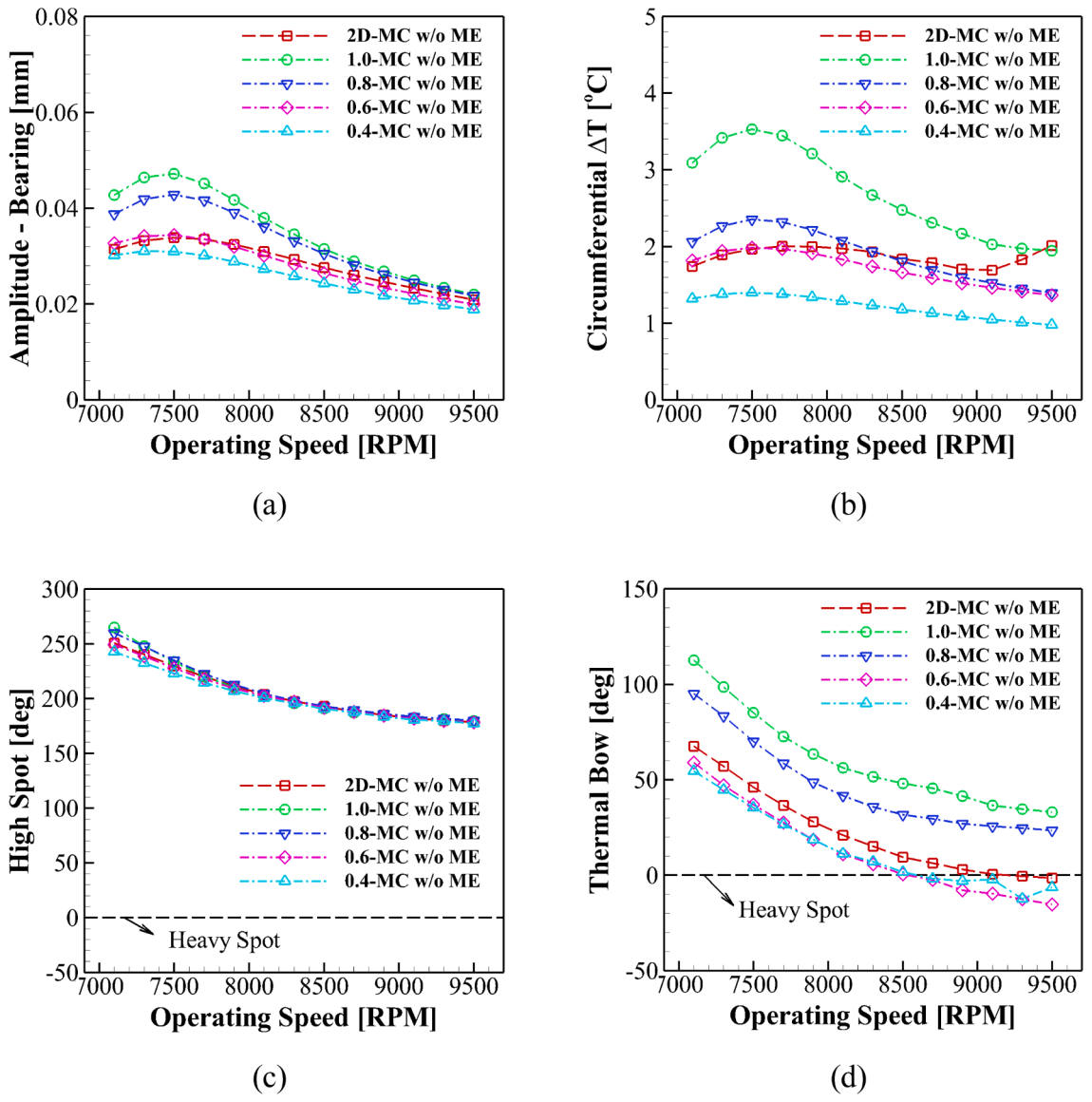

Fig. 11. Dynamic simulation results (w/o ME) for Case A injection; (a) amplitude at bearing (1x, peak-to-peak), (b) ΔT, (c) high spot, (d) thermal bow (hot spot – 180 deg); *2D-MC obtained from Case-A injection.

3.3.2. Oil injection type effect

The effect of TPJB oil injection type on the ME is presented here utilizing the proposed 2D-MC approach. The types are repeated here for convenience:

(1) Case-A: 1 small orifice ($D_g/W_g = 0.169$), closed-end seal, in Fig. 6(a), (mixed)
(2) Case-B: 1 large orifice ($D_g/W_g = 0.357$), closed-end seal, in Fig. 6(a), (flooded)
(3) Case-C: 1 nozzle ($D_g/W_g = 0.282$), open-end seal, in Fig. 6(b), (direct)
(4) Case-D: 3 nozzles ($D_g/W_g = 0.171$), open-end seal, in Fig. 6(c), (direct)

Fig. 13 presents the dynamic simulation results obtained in like manner with Section 3.3.1. The vibration magnitude in Fig. 13(a) and ΔT in Fig. 13(b) show similar trends. The distinctly larger value of the results compared with "Case-A w/o ME" in Fig. 11 indicates occurrence of a ME event. The ME occurrence speed range of Case-C is seen to be narrower than that of the others. From these results, Case-C may be the best method to reduce the ME symptoms. This assumes that the operating speed is in the upper, ME-free speed range, and the lower speed range can be traversed without encountering the ME. Case-C is a direct lubrication type with one nozzle and an open-end seal as depicted in Fig. 6(b). Case-D is also a direct lubrication type, but with three nozzle and an open-end seal as depicted in

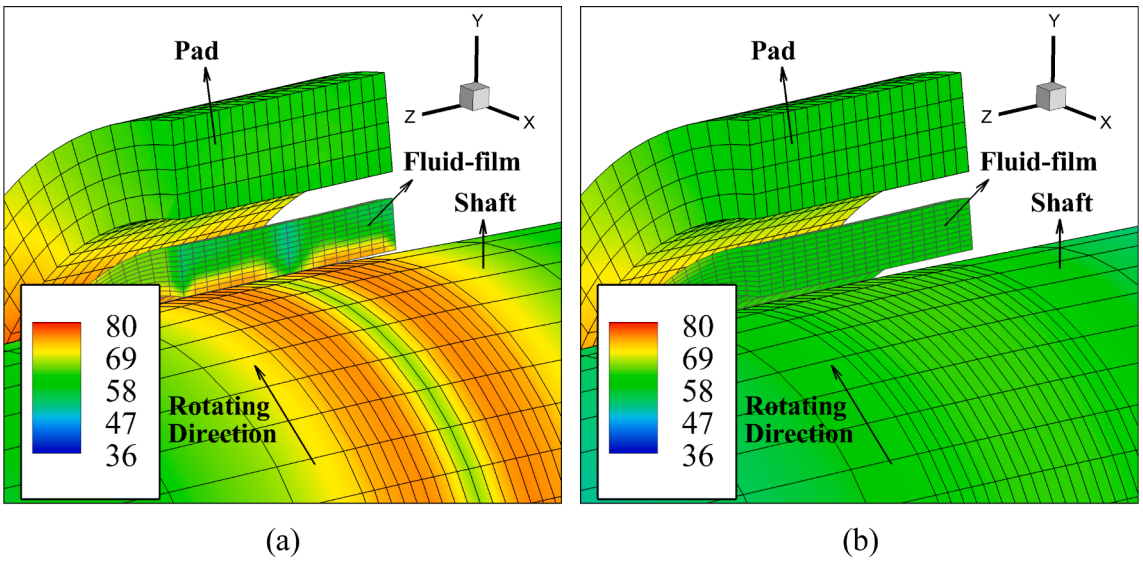

Fig. 12. Time averaged temperature contours near fluid-film leading-edge at 20 min (w/o ME, 8500 RPM); (a) 2D-MC, (b) 0.4-MC; *2D-MC obtained from Case-A injection.

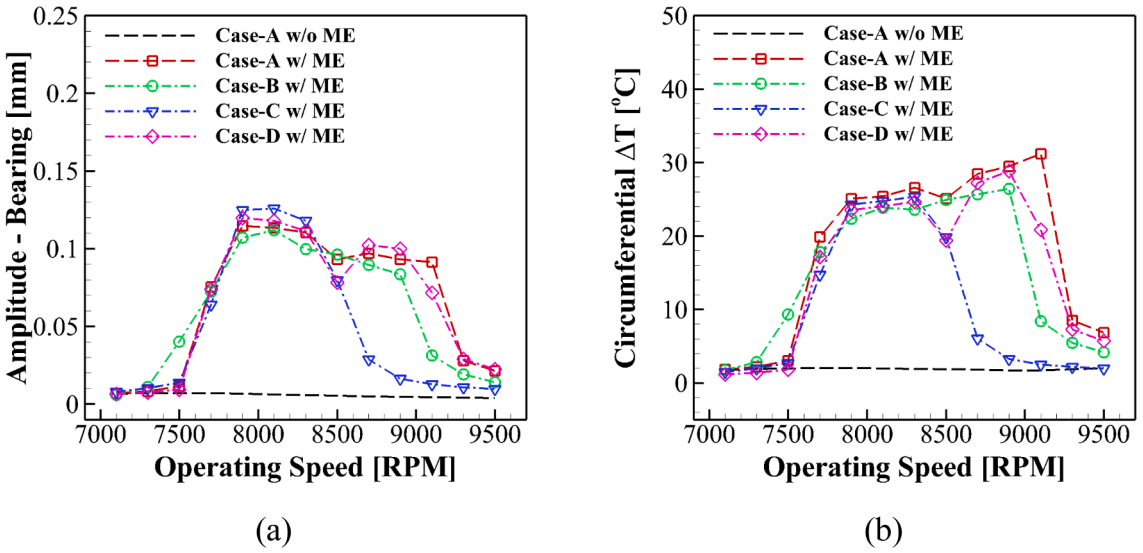

Fig. 13. Dynamic simulation results for injection Case-A – Case-D; (a) amplitude at bearing (1x, peak-to-peak), (b).ΔT.

Fig. 6(d). Fig. 13 shows that Case D has a much larger speed range with ME than Case C, and yet both are direct lubrication. This suggests that direct lubrication is not necessarily a remedy for suppressing the ME. Case-B with flooded lubrication, one orifice and a closed-end seal is slightly better than Case D for ME suppression.

Fig. 13 shows transient simulation results at 20 min or the time of encountering near rub. Fig. 14 shows the transient responses vs time at a constant speed of 9100 rpm, for oil injection types A – D. The results at the end of the transient simulation (20 min) clearly illustrate the different final amplitudes shown in Fig. 13.

Fig. 14(a)–(c) show the slow growth of vibration magnitude and ΔT with time due to the large thermal mass (time constant) of the rotor-bearing system. Case-A, which adopts mixed lubrication, shows the most severe ME instability, and reaches a near rub state near 16 min. The Case-D response reaches an impending near rub state near the end of the 20 min transient. In contrast, Case-C and Case-B exhibit steady, possibly acceptable responses at the end of the transient. The Case-B response is clearly the best injection type for suppressing ME.

Fig. 14(d)–(f) show the heavy, high, hot, and thermal bow angles to assist in understanding the ME mechanism for the 4 lubrication injection types. The heavy spot (applied mass imbalance weight) is located at 0 deg, and it leads the high spot (min film thickness) when the thermal bow effect is negligible at the start of the transient simulation, as discussed in Section 3.1. Consistent with operating

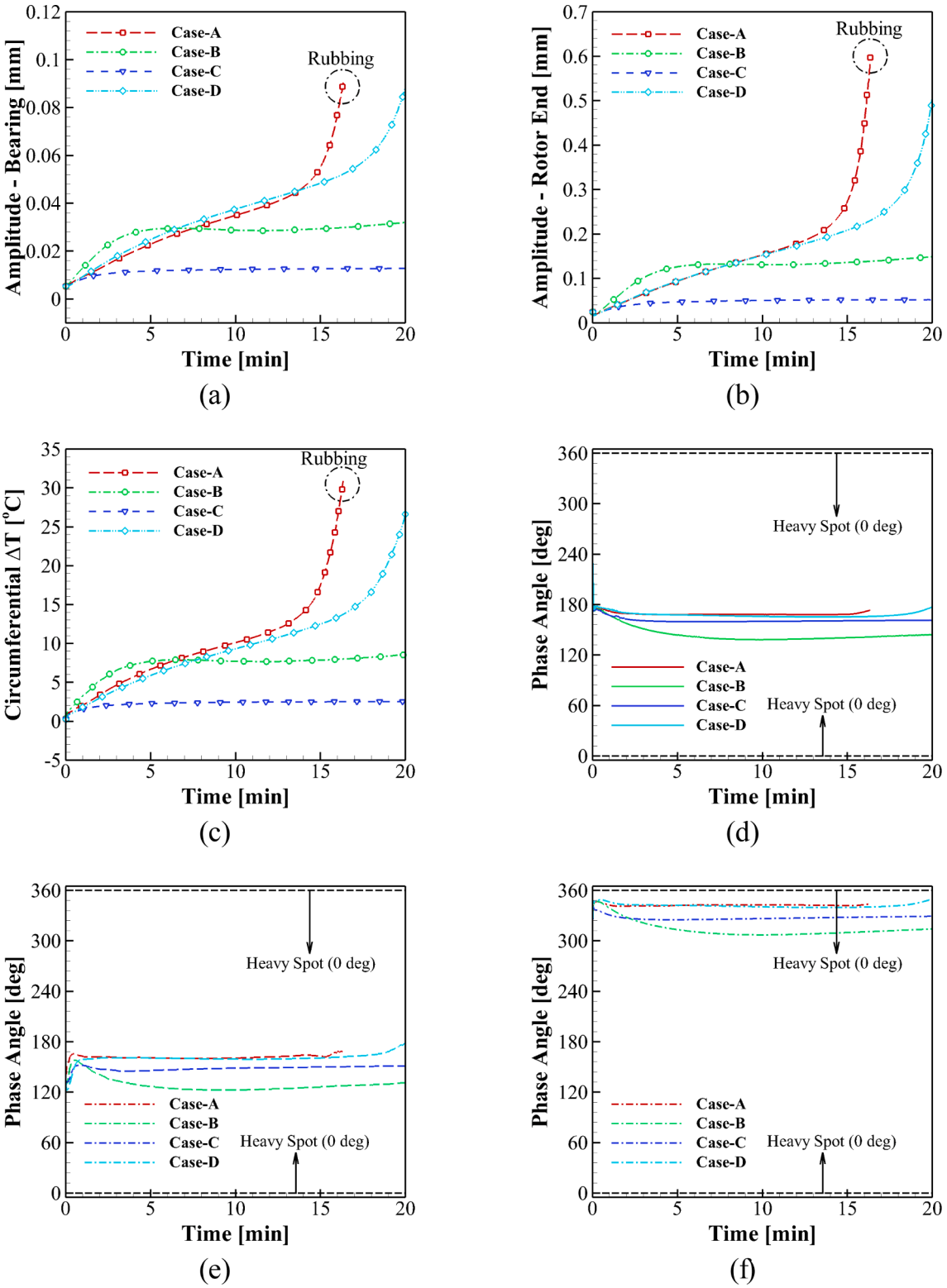

Fig. 14. Dynamic simulation results for Case-A – Case-D (w/ ME, 9100 RPM); (a) amplitude at bearing (1x, peak-to-peak), (b) amplitude at rotor-end, (c) ΔT, (d) heavy, high spot, (e) hot spot, (f) thermal bow.

well above resonance, the heavy spot leads the high spot by nearly 180 deg in all injection types near the start of the transient. This results since the thermal bow is negligible compared with the applied imbalance for all cases during the initial part of the transient simulation. The hot spot tends to track the high spot (minimum film thickness), and the high and hot spots continuously change as the thermal bow changes causing the resultant imbalance (applied plus bow induced) to vary. The thermal bow is positioned approximately 180 degrees from the hot spot. The severe ME shown in Fig. 14(a) – (c) for Cases A and D are consistent with their respective thermal bows being close to the heavy spot, yielding an increased resultant (equivalent) imbalance state. In contrast the thermal bows for cases B and C are displaced further from the heavy spot, yielding stable, relatively lower amplitude responses. The Case-C thermal bow–heavy spot angle separation is smaller than for case-B, yet its vibration amplitude is smaller. Fig. 14(c) explains this by showing a much smaller ΔT for Case-C, than for Case-B.

Fig. 15 shows the structure temperature contours, and heavy, hot, and high spots, and thermal bow at 15 min 20 *sec*, at an operating speed of 9,100 RPM. The intent of the Figure is to illustratively explain the relative severity of the ME between the 4 oil injection types. The contours are for temperatures that are time averaged over 1 entire revolution of the shaft.

The heavy spot (applied mechanical imbalance) is located at 0 deg for all cases. The thermal bow angle is also shown, and the resultant of the heavy spot imbalance and the "equivalent" thermal bow imbalance lies somewhere between the two. The propensity for severe ME effect occurrence becomes more acute as the thermal bow and heavy spot locations become more coincident, as is illustrated for Cases A and D, in Fig. 15(a) and (d). Severe ME synchronous vibration is confirmed in Fig. 14 for these cases. Conversely,

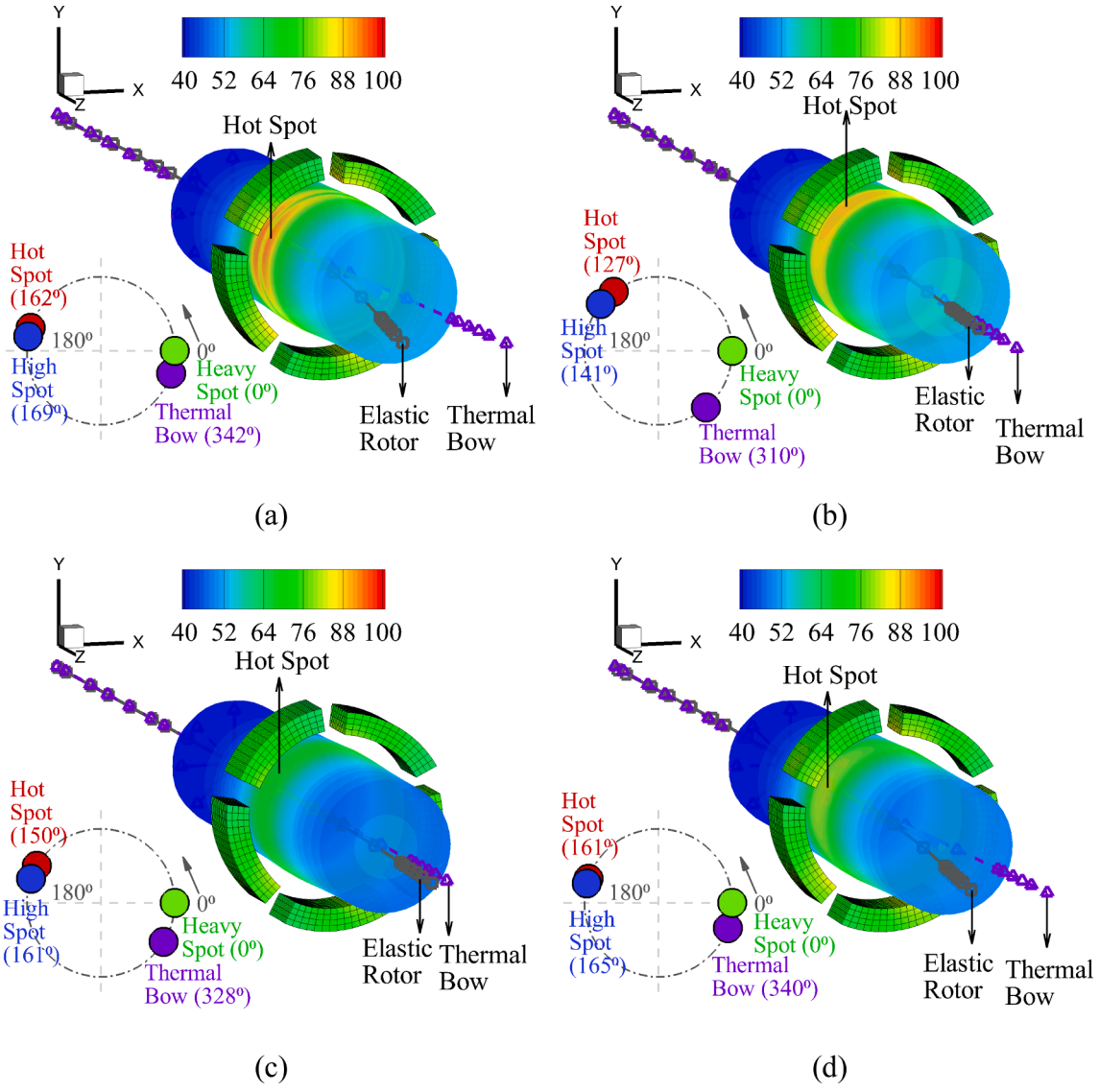

Fig. 15. Time averaged temperature contour for solid domains and heavy, hot, high spots, and thermal bow depiction at 9100 RPM ($t = 15$ min and 20 *sec*); (a) Case-A, (b) Case-B, (c) Case-C, (d) Case-D.

Fig. 15(b) and (c) show that the heavy spot and thermal bow angles are widely separated for injection types B and C. Bounded, stable ME synchronous vibration is confirmed in Fig. 14 for these cases.

The journal temperatures provided in Figs. 14 and 15 also illustrate some informative aspects about the ME. Fig. 15 shows a clear difference in journal temperature distributions depending on oil injection type utilized. Fig. 15 shows that Case-A and Case-B have markedly higher temperatures than Case-C and Case-D. However, Fig. 14 shows that $\Delta\Delta T$ is relatively higher in Case-A and Case-D, both of these cases have a severe ME response, and Case-B and Case-C have bounded, stable ME. This illustrates that higher overall journal temperature may not assure higher ΔT, and therefore may not be a good indicator of ME likelihood.

Fig. 16 presents a zoomed in view of the time averaged temperature distributions as the journal hot spot approaches the leading edge of pad 4 in Fig. 2. Fig. 16(a) shows the 2D-MC model temperature contours for the Case-A injection type. The fluid film temperature at the pad leading edge equals the between-pad region exit temperatures as provided by the CFD trained ANN. This clearly indicates the cooler region near the oil supply inlet (orifice) and side outlets, and higher temperature near the journal surface. The higher temperature near the journal surface at the pad leading edge is also observed for Case-B, in Fig. 16(b). The radial temperature distribution exiting the between-pad region at the fluid-film leading-edge produces the relatively higher journal temperature in Case-A and Case-B. Fig. 16(d) shows the cooling effect provided by the supply oil inlet (three nozzles) and side outlet for injection type Case-D. Fig. 16(c) shows a near uniform temperature distribution in the entire computational domain for Case-C, resulting in the steady, mild, bounded ME as shown in Fig. 14. Similar temperature patterns exists for all pads as illustrated for pad 4.

This section focused on the effects of oil injection type on the ME for the 4 types presented, as demonstrated in Figs. 13–16. The CFD trained ANN, 2D-MC model was employed for all results, having established in Section 3.3.1, with Figs. 10–12, that the constant MC model has significant variability of vibration amplitude, ΔT and thermal bow, depending on the choice of an uncertain MC. This was shown for both the w/o ME and w/ME simulations. This section demonstrated that the journal temperature distribution, ΔT, and thermal bow are significantly influenced by the oil injection type. Consequently, the ME vibration response is also influenced by the oil injection type ranging from a relatively small bounded vibration for Case-C, to a severe diverging vibration for Case-A and Case-D.

3.3.3. Supply oil flowrate effect

This section investigates the effect of supply oil flowrate for Case-A – Case-B oil injection types, utilizing the 2D-MC modeling approach. A prior study [17] simulated the effect of the supply oil flowrate on the ME, but varying injection types was not considered, and 2D-MC was not included. Fig. 17 shows the dynamic simulation results estimated by the time averaged values described in Section 3.3.1. The simulation input conditions are all identical with that in Section 3.3.2, but oil supply flowrates of 15 and 45 LPM are used as input of the surrogate groove model. The lower flowrate (15 LPM) was utilized for all cases in Sections 3.3.1 and 3.3.2. Fig. 17(c) and (d) show that the ME instability vibration magnitudes and ΔTs are mitigated for Case-C and Case-D, by increasing the oil flowrate. Case-C and Case-D are direct lubrication types indicating that increasing the oil supply flowrate with direct lubrication may mitigate severe ME. This point is reinforced by comparing ΔT for the w/o ME model at 7,700 rpm, as summarized in Table 5. The direct lubrication cases C and D show a 40 %–50 % drop in ΔT as compared with cases A and B.

4. Conclusion

The literature and industrial experience indicate a lingering incomplete understanding of the ME and its accurate simulation at the design and troubleshooting stages, as expressed in [26]. This is most clearly exemplified in the often expressed frustration of having identical machines, some having and some not having the ME. This implies that the ME is highly sensitive to small changes in design and operation parameters. The accuracy of approximate models may perform poorly in these circumstances, requiring high fidelity modeling. Prior research [9–11,17] has addressed this issue by increasing modeling fidelity, but results indicated a continuing need for more modelling detail, implemented in a manner practical for industrial usage. The present paper addresses a weakness in ME modelling that originates in the uncertainty of selecting a mixing coefficient MC, and its resulting uniform leading edge, oil film temperature distribution, for thermo-hydro-elasto TPJB modelling. The leading edge film temperature distribution is critical for accurate ME prediction due to its effect on asymmetric journal heating, a prime source of the ME. Results here show that this distribution is highly dependent on oil injection types, which was neglected in prior publications. Yang and Palazzolo [19] presented the TPJB deep learning 2D-MC model, via CFD-informed machine learning, and its improved response predictions were verified. This study focused on static response, and stiffness and damping coefficient prediction. The present paper extends this work for application to the ME, which requires prediction of an accurate asymmetric journal temperature distribution, and a coupled flexible shaft – TPJB system model, which may experience synchronous instability during a transient simulation.

The present study presents a new ME simulation model by combining the ME modelling approach in [16,17] and the deep learning 2D-MC model in [19]. A major contribution was illustrating the weakness of the conventional constant-MC approach, and providing ME responses for various oil injection types. This was performed using a novel 2D-MC, CFD trained deep learning algorithm to provide leading edge temperature distributions. The approach will be useful for original equipment design and field troubleshooting to mitigate the ME.

The major findings from the study of the proposed approach are summarized below.

- ME occurrence and severity are affected by the value of the MC used in the conventional constant MC, TPJB model, as shown in Fig. 10. In contrast, the 2D-MC, deep learning approach presented here internally determines the MC distribution, adaptively, throughout the ME transient simulation. Its accuracy is demonstrated by comparing predicted and measured speed dependence of the ME, as demonstrated in Table 3, which references [21].

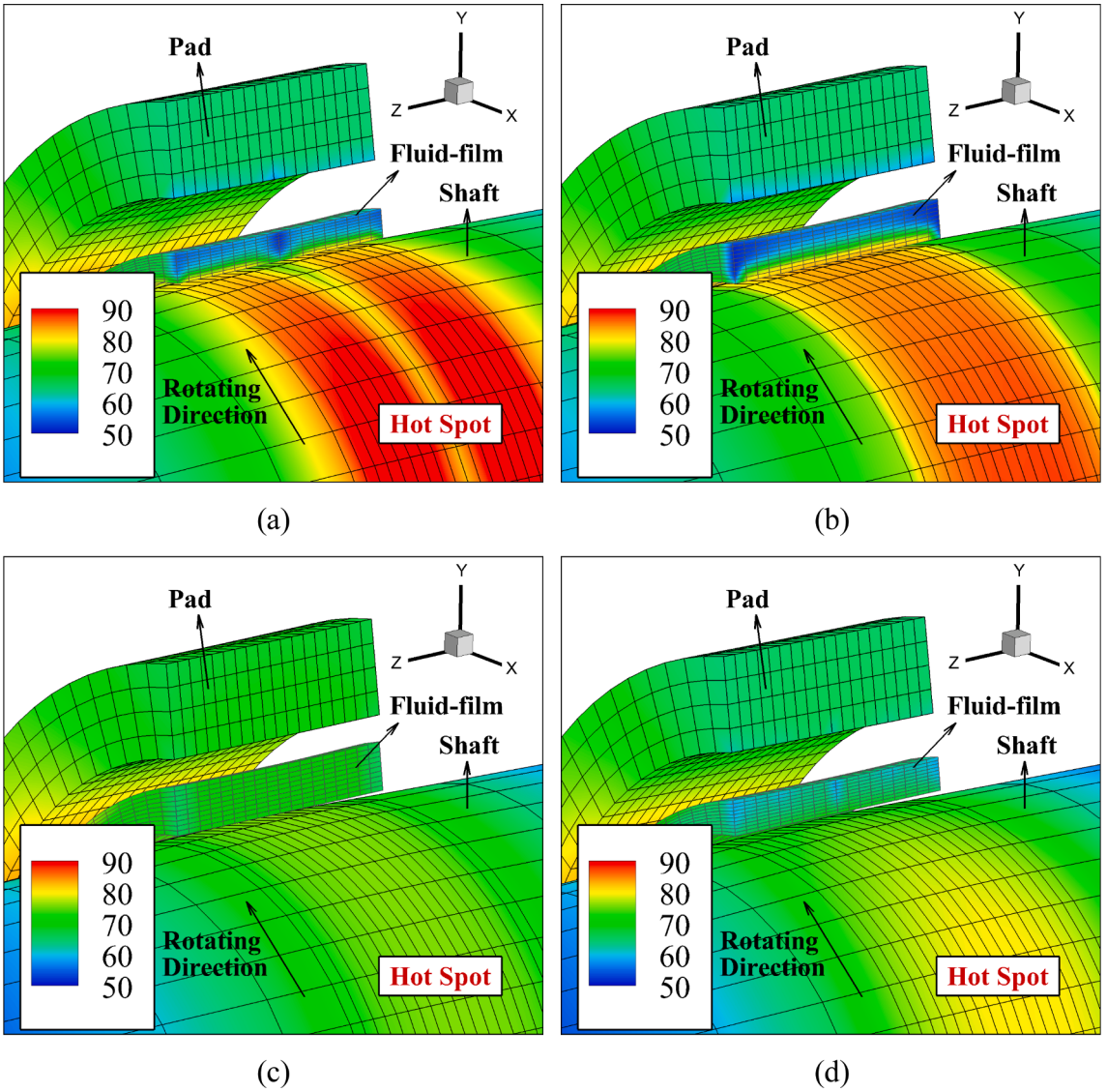

Fig. 16. Time averaged temperature contours near hot spot at 9100 RPM (15 min 20 *sec*); (a) Case-A, (b) Case-B, (c) Case-C, (d) Case-D.

- Simulations that calculate the thermal bow, but without feeding back the thermal bow as an excitation source "w/o ME", run economically. Care should be exercised though in extrapolating the results to the "w/ ME" simulation, which continuously updates thermal bow as a consequent of journal asymmetric heating, and as an excitation source. Fig. 11 shows by this approach low constant-MC's (0.4, 0.6) produce lower ΔT than the high constant-MCs (0.8, 1.0). However, Fig. 10 shows that low constant-MC's produce strong ME, and high constant-MCs do not cause a ME. This seemingly contradictory result is resolved by noting that the low constant-MC cases have thermal bow angles closer to the heavy spot as shown in Fig. 11(d). The weakness of the constant-MC approach is the strong sensitivity of 2 major determining factors for ME: ΔT and thermal bow angle to MC, and the high uncertainty of the MC values, which is generally selected based on limited experience or randomly.
- The ΔT, thermal bow and vibration amplitude show similar trends for both the low constant-MC (0.4, 0.6) and 2D-MC approaches, for the examples considered (Fig. 11). However, the low constant-MC approach is not recommended because as shown in Fig. 12 its temperature field can be very different from the 2D-MC, so the trend agreement in the present example may not extend in general to other rotor and bearing models.
- The oil injection type has a significant impact on the 2D-MC distribution (Fig. 7), and on the bearing and journal temperature distributions (Fig. 15 and Fig. 16). This affects the ΔT and thermal bow, and ultimately the ME system response (Fig. 13).
- Case-C, that is direct lubrication with one nozzle, has a narrower ME occurrence speed range than the other injection types when supplying either 15 or 45 LPM oil flowrate (Figs. 13 and 17). However, it should not be concluded that direct lubrication is a general

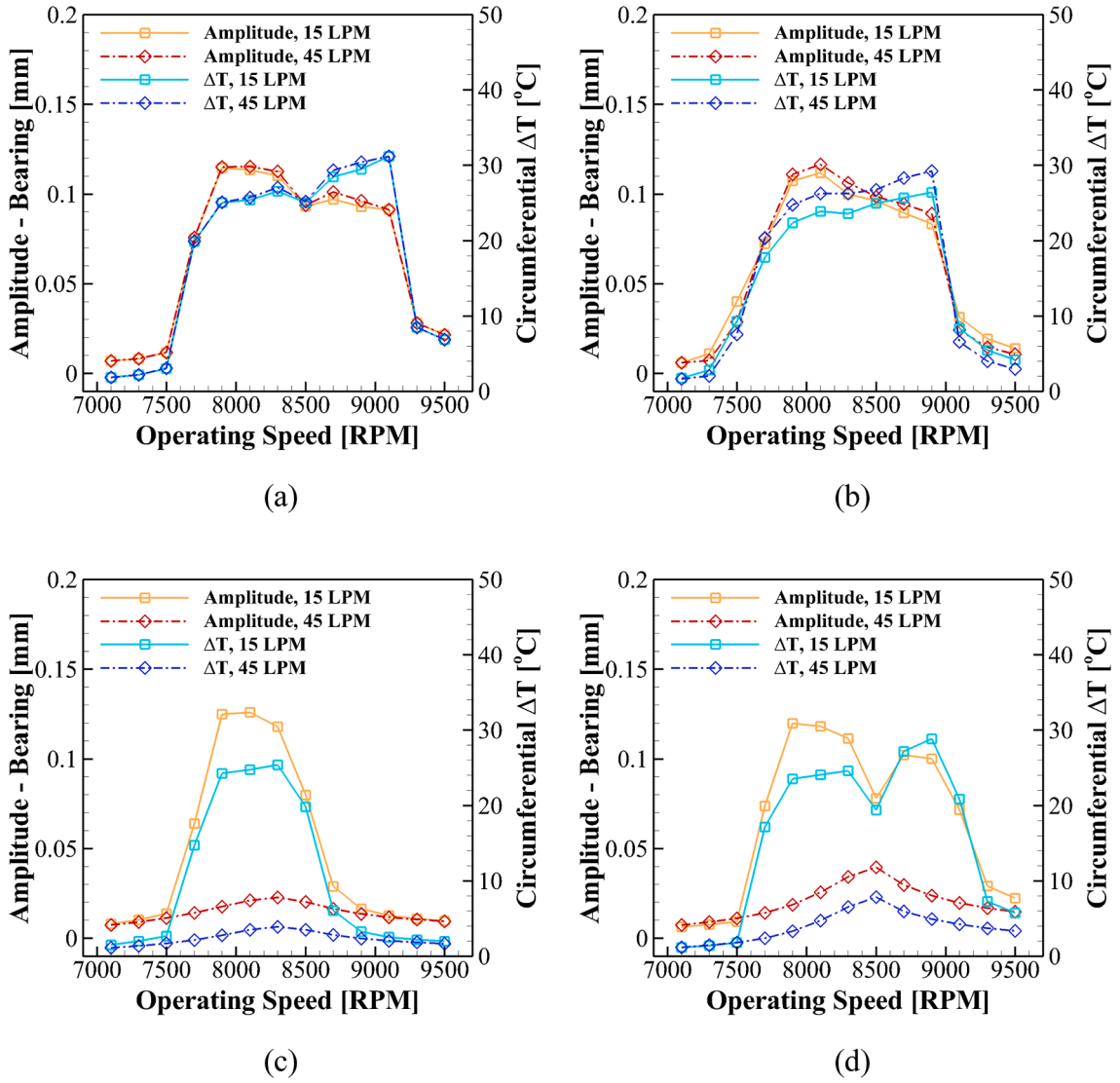

Fig. 17. Dynamic simulation results for increased supply oil flowrate in Case-A – Case-D oil injection types; (a) Case-A, (b) Case-B, (c) Case-C, (d) Case-D.

Table 5
Prior 2-min averaged results without thermal bow excitation (Supply oil flow: 45 LPM, Operating speed: 7,700 RPM).

Parameters	Amplitude at Bearing [um]	Circumferential ΔT [°C]	Approximate Thermal Bow Angle [deg]
Case-A	6.85	2.00	36.5
Case-B	6.75	1.86	34.5
Case-C	6.80	1.05	30.1
Case-D	6.71	1.15	31.0

* Approximate Thermal Bow Angle = Hot spot – 180 [deg].

remedy to remove the ME, since Case-D (three nozzles) which also employs direct lubrication showed more severe ME than Case-B (one orifice) with flooded lubrication.

- The effect of oil supply flowrate on ME was evaluated for the Case A – Case-D oil injection types. Simulating an intense oil flowrate (45 LPM) mitigated ME for the direct lubrication types (Case-C and Case-D) while not affecting the ME for the Case-A and Case-B types (Fig. 17). The ME mitigation results from a 40 % – 50 % decrease in ΔT with the high oil supply flowrate, since the thermal bow angle is only slightly changed (Table 5).

Declaration of Competing Interest

The authors declare that they have no known competing financial interests or personal relationships that could have appeared to influence the work reported in this paper.

Data availability

Data will be made available on request.

Acknowledgment

The authors acknowledge the generous funding provided by the Texas A&M University TEES Turbomachinery Research Consortium (TRC). Gratitude is also extended to the Texas A&M High Performance Research Computing Center.

References

[1] Morton, P. G., 1975, "Some Aspects of Thermal Instability in Generators," G.E.C. Internal Report No. S/W40 u183.
[2] Hesseborn, B., 1978, "Measurements of Temperature Unsymmetries in Bearing Journal Due to Vibration," Internal Report ABB Stal.
[3] P. Keogh, P. Morton, Journal bearing differential heating evaluation with influence on rotor dynamic behaviour, Proc. R. Soc. London, Ser. A 441 (1913) (1993) 527–548.
[4] P. Keogh, P. Morton, The dynamic nature of rotor thermal bending due to unsteady lubricant shearing within a bearing, Proc. R. Soc. London, Ser. A 445 (1924) (1994) 273–290.
[5] R. Gomiciaga, P. Keogh, Orbit Induced Journal Temperature Variation in Hydrodynamic Bearings, ASME J. Tribol. 121 (1) (1999) 77–84.
[6] A.C. Balbahadur, R. Kirk, Part I—Theoretical Model for a Synchronous Thermal Instability Operating in Overhung Rotors, Int. J. Rotating Mach. 10 (6) (2004) 469–475.
[7] A.C. Balbahadur, R. Kirk, Part II—Case studies for a synchronous thermal instability operating in overhung rotors, Int. J. Rotating Mach. 10 (6) (2004) 477–487.
[8] D. Childs, R. Saha, A new, iterative, synchronous-response algorithm for analyzing the morton effect, ASME J. Eng. Gas Turbines Power 134 (7) (2012), 072501.
[9] J. Suh, A. Palazzolo, Three-dimensional thermohydrodynamic morton effect simulation—Part I: theoretical model, ASME J. Tribol. 136 (3) (2014), 031706.
[10] J. Suh, A. Palazzolo, Three-dimensional thermohydrodynamic morton effect analysis—Part II: parametric studies, ASME J. Tribol. 136 (3) (2014), 031707.
[11] X. Tong, A. Palazzolo, J. Suh, Rotordynamic morton effect simulation with transient, thermal shaft bow, ASME J. Tribol. 138 (3) (2016), 031705.
[12] Plantegenet, T., Arghir, M., Hassini, M., and Jolly, P., "The Thermal Unbalance Effect Induced by a Journal Bearing in Rigid and Flexible Rotors: Experimental Analysis," Tribol. Trans., 63(1), pp.52-67.
[13] Plantegenet, T., Arghir, M., and Jolly, P., "Experimental analysis of the thermal unbalance effect of a flexible rotor supported by a flexure pivot tilting pad bearing," Mech. Syst. and Signal Process., 145, pp. 106953.
[14] C. Ettles, Hot oil carry-over in thrust bearings, Proc. Inst. Mech. Eng., Conf. Proc. 184 (12) (1969) 75–81.
[15] J. Mitsui, H. Hori, M. Tanaka, Thermohydrodynamic analysis of cooling effect of supply oil in circular journal bearing, ASME J. Lubr. Tech. 105 (3) (1983) 414–420.
[16] J. Yang, A. Palazzolo, Tilt pad bearing distributed pad inlet temperature with machine learning—Part I: static and dynamic characteristics, ASME J. Tribol. 144 (6) (2021), 061801.
[17] J. Yang, A. Palazzolo, Tilt pad bearing distributed pad inlet temperature with machine learning—part II: morton effect, ASME J. Tribol. 144 (6) (2021), 061802.
[18] J. Yang, A. Palazzolo, CFD based machine learning mixing prediction for tilt pad journal bearing TEHD -Part II: implementation with machine learning, ASME J. Tribol. 143 (1) (2020), 011802.
[19] J. Yang, A. Palazzolo, Deep convolutional autoencoder augmented cfd thermal analysis of bearings with inter pad groove mixing, Int. J. Heat Mass Transf. 188 (6) (2022), 122639.
[20] De Jongh, F., and Van Der Hoeven, P., eds., 1998, "Application of a Heat Barrier Sleeve to Prevent Synchronous Rotor Instability," 27th Turbomachinery Symposium, Houston, TX, Sept. 20–24, pp. 17–26.
[21] J. Yang, A. Palazzolo, 3D thermo-elasto-hydrodynamic CFD model of a tilting pad journal bearing-part i: static response, ASME J. Tribol. 141 (6) (2019), 061702.
[22] K. He, X. Zhang, S. Ren, J. Sun, Delving deep into rectifers: surpassing humanlevel performance on imagenet classifcation, in: Proceedings of the IEEE International Conference on Computer Vision, 2015, pp. 1026–1034.
[23] J. Yang, A. Palazzolo, CFD based machine learning mixing prediction for tilt pad journal bearing TEHD modeling -part i: model validation and improvements, ASME J. Tribol. 143 (1) (2020), 011801.
[24] T. Hagemann, H. Schwarze, Theoretical and experimental analyses of directly lubricated tilting-pad journal bearings with leading edge groove, ASME J. Eng. Gas Turbines Power 141 (5) (2019), 051010.
[25] Tong, X., and Palazzolo, A., "Measurement and Prediction of the Journal Circumferential Temperature Distribution for the Rotordynamic Morton Effect," ASME J. Tribol., 140(5), 031702.
[26] X. Tong, A. Palazzolo, J. Suh, A review of the rotordynamic thermally induced synchronous instability (morton) effect, ASME Appl. Mech. Rev. 69 (2017), 060801.